THE ASTROPHYSICAL JOURNAL, 928:87 (21pp), 2022 March 20 https://doi.org/10.3847/1538-4357/ac5024

The Strongest Cluster Lenses: An Analysis of the Relation between Strong Gravitational Lensing Strength and the Physical Properties of Galaxy Clusters

Carter Fox, Guillaume Mahler, Keren Sharon, and Juan D. Remolina González
Department of Astronomy, University of Michigan, 1085 South University Ave., Ann Arbor, MI 48109, USA; carfox@umich.edu

Received 2021 April 1; revised 2021 December 5; accepted 2022 January 28; published 2022 March 29

Abstract

Strong gravitational lensing provides unique opportunities to investigate the mass distribution at the cores of galaxy clusters and to study high-redshift galaxies. Using 110 strong-lensing models of 74 cluster fields from the Hubble Frontier Fields (HFF), Reionization Lensing Cluster Survey (RELICS), and Sloan Giant Arcs Survey (SGAS), we evaluate the lensing strength of each cluster (area with $|\mu| \geqslant 3$ for $z_s = 9$, normalized to a lens redshift of $z = 0.5$). We assess how large-scale mass, projected inner-core mass, and the inner slope of the projected mass-density profile relate to lensing strength. While we do identify a possible trend between lensing strength and large-scale mass (Kendall $\tau = 0.26$ and Spearman $r = 0.36$), we find that the inner slope (50 kpc $\leqslant r \leqslant$ 200 kpc) of the projected mass-density profile has a higher probability of correlation with lensing strength and can set an upper bound on the possible lensing strength of a cluster (Kendall $\tau = 0.53$ and Spearman $r = 0.71$). As anticipated, we find that the lensing strength correlates with the effective Einstein area and that a large ($\gtrsim 30\farcs0$) radial extent of lensing evidence is a strong indicator of a powerful lens. We attribute the spread in the relation to the complexity of individual lensing clusters, which is well captured by the lensing-strength estimator. These results can help us to more efficiently design future observations to use clusters as cosmic telescopes.

Unified Astronomy Thesaurus concepts: Galaxy clusters (584); Strong gravitational lensing (1643)

1. Introduction

Clusters of galaxies are located at the nodes of the cosmic filaments and represent the densest structures of dark matter; their merging history and evolution shape the properties of their mass distribution. The density profiles of massive galaxy clusters show strong self-similarity up to $z \sim 2$ outside of cluster cores (McDonald et al. 2017), but depart from this self-similarity within cluster cores. These high-density core regions are also where evidence of strong lensing is observed in clusters above a characteristic density, in the form of multiple instances of magnified and distorted images of lensed galaxies—dubbed arcs, or giant arcs.

Strong-lensing galaxy clusters can play a key role in our understanding of the universe, from mapping the distribution of matter in its densest regions, to the study of the earliest galaxies that they magnify.

An apparent discrepancy between the observed and expected number of giant arcs, known as the "arc statistics problem," has motivated studies of the correlation among strong-lensing efficiency, cosmology, and cluster properties (see Meneghetti et al. 2013 for a review). Cosmological analyses reveal that the number of giant arcs is sensitive to Ω_m and σ_8 (Wambsganss et al. 2008; Li et al. 2006; Fedeli et al. 2008; Oguri & Blandford 2009; Boldrin et al. 2016), self-interacting dark matter cross sections (Meneghetti et al. 2001; Wyithe et al. 2001), primordial non-Gaussianity (Oguri & Blandford 2009; D'Aloisio & Natarajan 2011), and dark energy (Bartelmann et al. 2003; Meneghetti et al. 2005). Giocoli et al. (2012) found that halo concentration is the most important factor for the lensing cross sections for production of large arcs, with more concentrated halos having larger strong-lensing cross sections. Xu et al. (2016) claim that the cluster mass-concentration relation could be the main driver of the lensing efficiency. Observations of strong-lensing clusters (Gladders et al. 2003) suggest that they might belong to a subpopulation of clusters with especially high lensing cross sections, which could explain the excess of observed arcs. Salmon et al. (2020) found little to no correlation between total cluster mass and the number of lensed high-z ($z \sim 6$–8) candidates, across a large survey of massive clusters. Evidence is therefore emerging that the properties that contribute to strong-lensing cross sections are both numerous and complex.

By leveraging the ability of lensing clusters to magnify the background universe, the search for high-redshift galaxies has become a particular interest in recent years (for a broad review, see Kneib & Natarajan 2011). It is the main science goal of projects like Hubble Frontier Fields (HFF; Lotz et al. 2017) and the Reionization Lensing Cluster Survey (RELICS; Coe et al. 2019), and of particular interest in preparation for the James Webb Space Telescope. It is therefore imperative to identify predictors of lensing strength, to increase our efficiency in selecting the best cosmic telescopes for follow-up.

Surveys to identify, catalog, and study the lines of sight of strong-lensing clusters—either for cluster science or for their use as cosmic telescopes—employ two major discovery approaches: lensing-selected and non-lensing-selected. Lensing-selected surveys rely on inspection of relatively shallow, large data sets to identify instances of strong-lensing evidence (e.g., Sloan Digital Sky Survey (SDSS), Sharon et al. 2020; Dark Energy Survey, Diehl et al. 2017), usually in the form of highly magnified bright giant arcs. The second approach is to examine deep or high-resolution optical imaging data of galaxy clusters that were selected for follow-up observation based on some criteria, usually high total mass as indicated from optical, X-ray, or submillimeter mass proxies. Examples of such surveys include the follow-up of the MAssive Cluster Survey (MACS; Ebeling et al. 2001), the South Pole Telescope clusters (HST SNAP 16017; PI: Gladders), the Local Cluster Substructure Survey (LoCuSS; Smith et al. 2005), and the Red-Sequence Cluster Survey (RCS; Gladders & Yee 2005). Both approaches can use either manual or machine-assisted identification of lensing evidence.

In this paper we investigate the relation between physical cluster properties and lensing strength, in order to assess some of the commonly used indicators and identify new indicators of strong-lensing efficiency. We base our investigation on a large sample of observed strong-lensing clusters at a wide range of redshifts and masses. Our study combines a total of 110 strong-lensing models of 74 cluster fields. Discerning the most important cluster properties for lensing efficiency enhances our understanding of galaxy clusters, and aids in the design of future surveys for cluster lenses.

This paper is organized as follows. In the remainder of the introduction, we review previous work related to proxies of lensing efficiency. In Section 2, we describe the sample of strong-lensing models that we use for our analysis. In Section 3, we discuss our methods, define the lensing-strength indicator and the cluster properties used in our analysis (large-scale mass, core mass, inner slope, effective Einstein area, and the distance to the farthest bright arc). In Section 4, we present and discuss our results. We conclude in Section 5. Throughout this paper, we adopt a standard ΛCDM cosmology with $\Omega_m = 0.3$, $\Omega_\Lambda = 0.7$, and $h = 0.7$ for models based on the `Lenstool`, Light-Traces-Mass, GRALE, and GRAVLENS methods. GLAFIC-based models of clusters included in the RELICS program use the parameters found by the Wilkinson Microwave Anisotropy Probe (Komatsu et al. 2011), with $\Omega_m = 0.272$, $\Omega_\Lambda = 0.728$, and $h = 0.704$. We refer the interested reader to Bayliss et al. (2015) for an assessment of the impact of cosmological parameter uncertainties on mass and magnification errors. M_Δ refers to the 3D mass within the radius at which the average density is Δ times the critical density of the universe at the redshift of the cluster.

1.1. Contributors to Strong-lensing Efficiency

Numerous studies endeavored to identify key lens characteristics that influence strong-lensing efficiency, usually coded as the abundance of lenses, or the appearance, distributions, or properties of giant arcs.

There is a general agreement in the literature that for a given total cluster mass, strong lenses are expected to be more highly concentrated (e.g., Meneghetti et al. 2013; Miralda-Escude 1995; Molikawa & Hattori 2001; Oguri et al. 2001; Fedeli et al. 2007; Gralla et al. 2011; Giocoli et al. 2012; Saez et al. 2016; Oguri et al. 2001). The slope of the mass distribution affects not only the abundance of strong-lensing features, but also the lensing configuration; flat inner profiles are found to produce images that are less distorted (Futamase et al. 1998; Williams & Lewis 1998; Morioka & Futamase 2015).

The geometry of the lensing halo also plays a role in increasing the strong-lensing power. Meneghetti et al. (2003, 2007) show that the ellipticity of the lens affects its lensing efficiency, and might have a higher impact than asymmetries and substructures on boosting the lensing signal. Hennawi et al. (2007) report that triaxiality increases the number of giant arcs compared with spherically symmetric halos that fail to reproduce the lensing signal (Dalal & Keeton 2003; Bartelmann & Meneghetti 2004). Studies comparing simulations and observations (Dalal et al. 2004; Horesh et al. 2005) show that realistic triaxiality and substructure can reproduce the observed lensing signal at low-redshift clusters, claiming that the discrepancy at higher redshift is due to the redshift dependence of the cluster mass function. Moreover, an alignment of the major axis of a triaxial halo along the line of sight would increase the projected mass slope of the inner profile (Meneghetti et al. 2003, 2007) and thus increase the strong-lensing efficiency.

Although the dark matter component dominates the cluster mass, its galaxies and baryonic components have a non-negligible effect, directly or indirectly, on its lensing cross section. Studying the cluster stellar component, Hilbert et al. (2008) show that a higher level of substructure increases lensing efficiency. Ho & White (2005) show in simulated clusters that the lensing cross section increases with the mass of the central cluster galaxy. However, these cluster properties are not independent of each other, and may work in opposite directions: for example, Richard et al. (2010) present observational evidence that as the central galaxy grows, the mass fraction of substructures and their stellar mass content diminishes.

Physical processes, such as baryonic cooling, influence the mass profile (Rozo et al. 2008; Wambsganss et al. 2008; Killedar et al. 2018) and have a potential to indirectly affect the lensing potential. Hilbert et al. (2008) found that adding the stellar component to dark matter simulation can boost the lensing signal, up to a factor of 2 for $10^{12} - 10^{13} M_\odot$ dark matter halos. Furthermore, Killedar et al. 2012 and Schaller et al. 2015b, 2015a found using simulation that active galactic nuclei feedback and baryonic physics at the core of the cluster could flatten the profile, effectively reducing strong-lensing efficiency, predominantly for the lowest mass clusters. Nevertheless, Blanchard et al. (2013) found no significant difference in the cooling signatures of the intracluster medium between lensing-selected and non-lensing-selected clusters.

Large-scale dynamical processes, such as cluster mergers, also influence lensing efficiency. The Einstein radii are larger in mergers, especially when the two merging cores are separated by $d < 0.3$Mpc (Redlich et al. 2012). This claim is confirmed by Torri et al. (2004), who demonstrate that the cross section for giant arcs can increase by an order of magnitude during the merging process, and that radial arcs are more common when substructure crosses the main cluster center.

Several studies highlighted aspects that may artificially affect the measured abundance of lensing incidents, and care should be taken when comparing observed lensing abundance and lens properties with theoretical predictions. Shape-based identification of arcs is sensitive to the distribution of intrinsic source shapes (e.g., Zaritsky & Gonzalez 2003), and to seeing (Cypriano et al. 2001), which circularizes the lensed images. The intrinsic morphology of the lensed galaxies can affect their detection efficiency in a way that may be redshift dependent. For example, Gladders et al. (2003) suggest that the clumpiness nature of sources at higher redshift might help to better identify lensing features in cluster observations and explain some of the discrepancy observed at higher redshifts between observations and theoretical predictions. Structure along the line of sight can boost the lensing cross section, decoupled from the properties of the main lensing plane. For example, Bayliss et al. (2014) found excess structure along the line of sight to strong-lensing clusters.

This paper builds upon these previous investigations. We focus our analysis on clusters that are already known to be strong lenses, with a wide range of total masses and redshifts. By selection, the projected mass density at the cores of these clusters exceeds the critical density for strong lensing, and they are likely drawn from the higher end of the concentration distribution for their mass. We define a lensing-strength indicator that may be less relevant to studies of arcs statistics, but instead is directly applicable to surveys that utilize strong-lensing clusters as cosmic telescopes.

2. Strong-lensing Models

This paper investigates how lensing strength relates to physical properties of galaxy clusters. We gather a sample of strong-lensing clusters with publicly available models from the HFF (Lotz et al. 2017), RELICS (Coe et al. 2019), and Sloan Giant Arcs Survey (SGAS; Sharon et al. 2020). The final sample, which consists of 74 cluster fields with a total of 110 lens models, spans a wide range in mass and redshift. Other repositories of strong-lensing clusters with public lens models are available in the literature. For example, the Cluster Lensing And Supernova survey with Hubble (CLASH; Postman et al. 2012) and Local Cluster Substructure Survey (LoCuSS; Smith et al. 2005; Richard et al. 2010) can be used in future work to complement this analysis. The four HFF clusters that are part of the CLASH sample are included in this work.

Table 1 lists the cluster fields used in this analysis and their relevant information. Figure 1 shows their mass–redshift distribution and in the Appendix we provide a gallery of color images for each cluster. We discuss the surveys from which the clusters we include in our sample were drawn and the publicly available lens models below.

Strong lens-modeling algorithms solve for the mass distribution in the lens plane, based on lensing evidence and modeling assumptions. The parametric approach models a cluster lens with a few large-scale components that represent one or more cluster scale dark matter halos, combined with small-scale components that use mass–luminosity relations to model galaxy scale halos. These halos are usually physically-motivated mass profiles, such as Navarro–Frenk–White (NFW; Navarro et al. 1997) or isothermal. “Free-form” models (also known as nonparametric) solve for the mass distribution with no underlying assumption on its radial dependence. Modeling algorithms also vary in their assumption of correlation between mass and light. Several modeling methods exist in the literature; we refer the interested reader to a recent comparison by Meneghetti et al. (2017). This paper uses models computed with several algorithms, for which public models are available: `Lenstool` (Jullo et al. 2007; Kneib et al. 1996; Jullo & Kneib 2009), Light-Traces-Mass (LTM; Zitrin et al. 2009), GLAFIC (Oguri 2010), GRALE (Liesenborgs et al. 2006; Mohammed et al. 2014), and GRAVLENS (Keeton 2001).

In some cases, we include in our analysis multiple models of the same cluster that were computed with different modeling algorithms. This approach may highlight systematic uncertainties that are not captured in the statistical modeling uncertainty of each model. We find that despite the differences between models, the results do not contradict the overall findings. None of the lens models used in this work includes multiplane lensing to account for possible structure along the line of sight. We note that while structures along the line of sight as well as difference in the choice of cosmology can influence the lensing potential, these perturbations only marginally affect our results.

2.1. Frontier Fields

The Hubble Frontier Fields (HFF; Lotz et al. 2017) is a Director’s Discretionary time campaign, using the Hubble Space Telescope (HST) and the Spitzer Space Telescope to obtain deep imaging data of six strong-lensing galaxy clusters. The science goal of this project is to study the high-z universe by combining the resolution power of HST and strong-lensing magnification in lines of sight of six massive clusters of galaxies. The strategy, of extremely deep multiband observations of each field, enables a high-completeness detection of cluster member galaxies and faint background sources. It resulted in the best constrained strong-lensing lines of sight to date, with hundreds of lensing constraints per field. Through extensive community effort, the strong-lensing potentials of these fields were modeled by several teams using different modeling approaches. The lens models are publicly available to the community on the Mikulski Archive for Space Telescopes (MAST)[1]. We use in our analysis public HFF lens models that satisfy the following criteria: the model is available on MAST as v4 or above (but see a comment below); provides a field of view large enough to encompass the region of interest for our work, where the magnification is $|\mu| \geqslant 3$ (see Section 3.1); and the maps provided have a resolution of $0\rlap{.}''4$ pixel^{-1} or better.

The models used in this work (see Table 1) are described in Johnson et al. (2014), Jauzac et al. (2016), Caminha et al. (2017), Lagattuta et al. (2019), Kawamata et al. (2016), Kawamata et al. (2018), and Raney et al. (2020a). We use the v4.1 (v4 when not available) lens models in all cases except for Abell 2744, where we use Sharon v3 and CATS v3.1, which are confined to the main cluster core and do not extend to the northwest structure (see Mahler et al. 2018). The largest differences usually appear in the lensing-strength values, which is expected. Meneghetti et al. (2017) show that for highly constrained clusters, such as the HFF clusters, the surface mass densities and magnifications show strong similarity across the different modeling techniques. Similarly, Remolina González et al. (2018) find excellent agreement between the v4 models of one of the HFF clusters. Raney et al. (2020b) highlight a 6% bias and 40% scatter at $|\mu| = 3$ that points to underestimation of statistical uncertainties of the HFF models.

2.2. RELICS

The Reionization Lensing Cluster Survey (RELICS; Coe et al. 2019) observed galaxy cluster fields, taking advantage of lensing magnification in order to detect galaxies at high redshifts ($z \gtrsim 6$). While its main science objective was similar to that of the HFF project, RELICS used a complementary strategy of a shallow survey with a large number of lines of sight to achieve its goals. RELICS observed 41 clusters with HST, more than half of which were selected from the Planck catalog for their high mass, based on an M_{500} estimate derived from the Sunyaev–Zel’dovich effect (SZ; Sunyaev & Zeldovich 1970). Known lensing features assisted the selection of the remaining clusters, as well as other mass estimates, such as X-ray and weak lensing (Coe et al. 2019).

Clusters observed in the RELICS program have been modeled by the RELICS team with three parametric modeling techniques: `Lenstool` (Jullo et al. 2007), LTM (Zitrin et al. 2009), and GLAFIC (Oguri 2010). The lens models are made

---

[1] https://doi.org/10.17909/T9KK5N

Table 1

All Clusters Included in this Paper, Separated by Strong-lensing Programs (HFF, RELICS, and SGAS)

Cluster	α J2000	δ J2000	$z_{\rm lens}$	M_{500} ($10^{14}M_\odot$)	M_{200} ($10^{14}M_\odot$)	Alg.	Spec-z	$M_{\rm SL}$(200kpc) ($10^{12}M_\odot$)	S_{50-200}	$e\theta_{\rm E}$ (arcsec)	$\mathcal{A}^{\rm lens}_{\lvert\mu\rvert\geqslant 3}$ (arcmin^2)	$\mathcal{A}^{0.5}_{\lvert\mu\rvert\geqslant 3}$ (arcmin^2)
HFF												
Abell 2744	3.586259	−30.400173	0.308	$12.44^{+1.42}_{-1.66}$	$19.40^{+2.66}_{-2.26}$	L-S[a]	yes	$179.69^{+2.00}_{-2.04}$	$-0.58^{+0.03}_{-0.03}$	$27.18^{+0.07}_{-0.09}$	$2.47^{+0.10}_{-0.10}$	$1.36^{+0.06}_{-0.05}$
						G[b]	yes	$180.79^{+1.33}_{-2.04}$	$-0.52^{+0.02}_{-0.03}$	$27.09^{+1.24}_{-0.34}$	$2.50^{+0.08}_{-0.10}$	$1.38^{+0.04}_{-0.05}$
						GL[c]	yes	$177.17^{+2.50}_{-3.41}$	$-0.51^{+0.03}_{-0.04}$	$26.15^{+0.25}_{-0.21}$	$3.37^{+0.25}_{-0.27}$	$1.86^{+0.14}_{-0.15}$
						GR	yes	$172.11^{+3.85}_{-4.07}$	$-0.62^{+0.06}_{-0.05}$	$30.74^{+4.03}_{-2.47}$	$2.58^{+0.15}_{-0.21}$	$1.43^{+0.08}_{-0.12}$
Abell 370	39.97133	−1.58224	0.375	$18.79^{+2.30}_{-2.30}$	$31.60^{+3.86}_{-3.86}$	L-S[a]	yes	$234.13^{+0.70}_{-1.82}$	$-0.46^{+0.01}_{-0.01}$	$44.80^{+0.00}_{-1.58}$	$5.62^{+0.08}_{-0.42}$	$4.02^{+0.05}_{-0.30}$
						L-CATS[d]	yes	$232.58^{+0.31}_{-0.53}$	$-0.48^{+0.01}_{-0.01}$	$43.54^{+0.02}_{-0.20}$	$4.58^{+0.02}_{-0.06}$	$3.27^{+0.02}_{-0.05}$
						GL[c]	yes	$231.60^{+1.16}_{-1.35}$	$-0.44^{+0.01}_{-0.01}$	$43.59^{+0.91}_{-0.39}$	$5.24^{+0.18}_{-0.25}$	$3.75^{+0.13}_{-0.18}$
Abell S1063	342.18321	−44.530894	0.348	$11.36^{+0.34}_{-0.34}$	$17.74^{+0.54}_{-0.54}$	L-S[a]	yes	$208.95^{+0.87}_{-0.83}$	$-0.61^{+0.02}_{-0.02}$	$36.79^{+0.23}_{-0.07}$	$3.99^{+0.06}_{-0.04}$	$2.59^{+0.04}_{-0.02}$
						L-CATS	yes	$203.40^{+1.63}_{-1.59}$	$-0.66^{+0.03}_{-0.02}$	$36.23^{+0.17}_{-0.16}$	$3.21^{+0.09}_{-0.07}$	$2.08^{+0.06}_{-0.05}$
						GL[c]	yes	$208.65^{+1.87}_{-2.36}$	$-0.62^{+0.02}_{-0.03}$	$36.65^{+0.23}_{-0.27}$	$4.05^{+0.17}_{-0.19}$	$2.63^{+0.11}_{-0.12}$
						GR	yes	$206.59^{+3.04}_{-2.82}$	$-0.55^{+0.09}_{-0.09}$	$37.92^{+1.56}_{-0.46}$	$2.55^{+0.05}_{-0.13}$	$1.66^{+0.03}_{-0.08}$
MACS J0416.1−2403	64.038078	−24.067497	0.396	$11.53^{+2.02}_{-2.18}$	$18.08^{+3.51}_{-3.24}$	L-S[a]	yes	$154.70^{+1.27}_{-0.82}$	$-0.51^{+0.01}_{-0.01}$	$32.26^{+0.04}_{-0.09}$	$2.28^{+0.07}_{-0.02}$	$1.74^{+0.05}_{-0.02}$
						L-Cam[e]	yes	$157.83^{+0.51}_{-2.21}$	$-0.44^{+0.01}_{-0.02}$	$31.09^{+0.59}_{-0.00}$	$2.45^{+0.04}_{-0.10}$	$1.87^{+0.03}_{-0.08}$
						L-CATS	yes	$158.50^{+1.50}_{-0.37}$	$-0.45^{+0.01}_{-0.03}$	$31.87^{+0.02}_{-0.23}$	$2.36^{+0.05}_{-0.03}$	$1.80^{+0.04}_{-0.02}$
						G[b]	yes	$147.14^{+3.60}_{-1.91}$	$-0.52^{+0.03}_{-0.02}$	$31.83^{+0.36}_{-0.02}$	$2.09^{+0.17}_{-0.10}$	$1.60^{+0.13}_{-0.08}$
						GL[c]	yes	$168.69^{+1.55}_{-5.22}$	$-0.41^{+0.02}_{-0.02}$	$32.65^{+0.20}_{-0.38}$	$3.05^{+0.05}_{-0.21}$	$2.33^{+0.04}_{-0.16}$
						GR	yes	$141.33^{+1.68}_{-1.05}$	$-0.61^{+0.04}_{-0.05}$	$32.79^{+0.61}_{-0.29}$	$1.64^{+0.03}_{-0.06}$	$1.25^{+0.03}_{-0.04}$
MACS J0717.5+3745	109.398239	37.745731	0.545	$11.49^{+0.53}_{-0.55}$	$18.24^{+0.86}_{-0.89}$	L-S[a]	yes	$234.73^{+1.53}_{-1.30}$	$-0.23^{+0.03}_{-0.02}$	$58.51^{+0.15}_{-0.47}$	$7.15^{+0.19}_{-0.10}$	$7.81^{+0.21}_{-0.11}$
MACS J1149.5+2223	177.39875	22.398533	0.543	$14.36^{+4.00}_{-4.30}$	$22.92^{+12.93}_{-15.19}$	L-S[a]	yes	$177.85^{+2.35}_{-0.36}$	$-0.51^{+0.01}_{-0.01}$	$30.74^{+0.33}_{-0.35}$	$4.19^{+0.18}_{-0.08}$	$4.56^{+0.20}_{-0.08}$
						L-CATS[f]	yes	$177.28^{+2.40}_{-1.00}$	$-0.52^{+0.02}_{-0.01}$	$32.71^{+0.63}_{-0.26}$	$3.35^{+0.23}_{-0.01}$	$3.65^{+0.24}_{-0.01}$
						GL[c]	yes	$173.96^{+6.55}_{-6.08}$	$-0.54^{+0.03}_{-0.03}$	$30.52^{+0.62}_{-0.53}$	$3.43^{+0.43}_{-0.39}$	$3.74^{+0.47}_{-0.42}$
						GR	yes	$170.78^{+2.87}_{-1.82}$	$-0.62^{+0.06}_{-0.07}$	$30.83^{+1.35}_{-0.04}$	$1.77^{+0.06}_{-0.13}$	$1.93^{+0.06}_{-0.14}$
RELICS												
Abell 1758a NW[g]	203.159975	50.55994	0.2799	$8.22^{+0.27}_{-0.28}$	$12.66^{+0.43}_{-0.44}$	G	unknown	$152.96^{+42.26}_{-6.67}$	$-0.59^{+0.06}_{-0.05}$	$24.84^{+1.02}_{-1.08}$	$2.51^{+1.15}_{-0.61}$	$1.20^{+0.55}_{-0.29}$
Abell 1758a SE[g]	203.21692	50.526126	0.2799			G	unknown	$147.88^{+37.70}_{-45.85}$	$-0.63^{+0.03}_{-0.22}$	$16.70^{+2.69}_{-3.92}$	$1.93^{+0.68}_{-1.33}$	$0.93^{+0.33}_{-0.64}$
Abell 2163	243.953949	−6.144829	0.203	$16.12^{+0.30}_{-0.29}$	$25.05^{+0.48}_{-0.46}$	L[h]	no	$107.04^{+20.16}_{-7.24}$	$-0.92^{+0.06}_{-0.04}$	$14.91^{+0.42}_{-0.11}$	$0.84^{+0.30}_{-0.19}$	$0.25^{+0.09}_{-0.06}$
						G	unknown	$168.45^{+52.51}_{-37.53}$	$-0.50^{+0.10}_{-0.20}$	$15.02^{+0.20}_{-0.51}$	$2.72^{+3.33}_{-1.62}$	$0.81^{+0.99}_{-0.48}$
Abell 2537	347.092607	−2.19217	0.2966	$5.52^{+0.51}_{-0.51}$	$8.43^{+0.80}_{-0.80}$	L[h]	yes	$202.99^{+2.90}_{-0.92}$	$-0.66^{+0.03}_{-0.02}$	$32.25^{+0.32}_{-0.15}$	$3.63^{+0.44}_{-0.15}$	$1.90^{+0.23}_{-0.08}$
						G	yes	$216.70^{+1.95}_{-16.67}$	$-0.51^{+0.02}_{-0.18}$	$33.61^{+0.12}_{-0.66}$	$6.22^{+0.35}_{-2.82}$	$3.23^{+0.18}_{-1.47}$
Abell 2813	10.852708	−20.628215	0.2924	$8.13^{+0.37}_{-0.38}$	$12.53^{+0.58}_{-0.60}$	L	yes	$168.54^{+4.95}_{-1.94}$	$-0.47^{+0.01}_{-0.02}$	$28.52^{+0.66}_{-0.02}$	$2.67^{+0.10}_{-0.10}$	$1.37^{+0.05}_{-0.05}$
Abell 3192	59.725312	−29.925271	0.425	$7.20^{+0.52}_{-0.50}$	$11.19^{+0.83}_{-0.80}$	L	yes	$184.14^{+4.58}_{-4.04}$	$-0.56^{+0.04}_{-0.01}$	$32.87^{+1.08}_{-0.14}$	$2.45^{+0.22}_{-0.10}$	$2.04^{+0.19}_{-0.09}$
Abell 697	130.739821	36.366498	0.282	$11.00^{+0.37}_{-0.37}$	$17.06^{+0.59}_{-0.59}$	LTM[i]	no	$58.97^{+12.66}_{-0.47}$	$-1.26^{+0.15}_{-0.03}$	$12.85^{+0.23}_{-0.13}$	$0.28^{+0.08}_{-0.04}$	$0.13^{+0.04}_{-0.02}$
Abell S295	41.353387	−53.029324	0.3	$6.78^{+0.37}_{-0.36}$	$10.41^{+0.58}_{-0.57}$	LTM[i]	yes	$146.14^{+18.36}_{-8.01}$	$-0.37^{+0.04}_{-0.08}$	$17.77^{+1.71}_{-0.46}$	$4.38^{+0.80}_{-0.49}$	$2.33^{+0.43}_{-0.26}$
ACT−CL J0102−49151	15.740679	−49.272001	0.87	$10.75^{+0.48}_{-0.47}$	$17.44^{+0.80}_{-0.78}$	L[h]	no	$182.56^{+22.63}_{-10.13}$	$-0.64^{+0.04}_{-0.07}$	$40.29^{+1.43}_{-0.77}$	$3.59^{+0.67}_{-0.74}$	$5.74^{+1.07}_{-1.18}$
						G	unknown	$179.71^{+42.76}_{-5.14}$	$-0.50^{+0.03}_{-0.09}$	$43.38^{+1.30}_{-1.93}$	$4.74^{+1.74}_{-0.87}$	$7.65^{+2.81}_{-1.41}$
CL J0152.7−1357	28.182425	−13.95515	0.833	…	…	L	yes	$119.09^{+7.96}_{-6.99}$	$-0.78^{+0.09}_{-0.06}$	$17.88^{+0.78}_{-0.68}$	$0.81^{+0.11}_{-0.09}$	$1.26^{+0.17}_{-0.13}$
						LTM[j]	yes	$115.24^{+21.01}_{-0.00}$	$-0.68^{+0.05}_{-0.02}$	$19.29^{+2.47}_{-0.76}$	$1.55^{+0.32}_{-0.00}$	$2.41^{+0.50}_{-0.00}$
						G	yes	$128.40^{+9.37}_{-15.82}$	$-0.55^{+0.01}_{-0.14}$	$18.32^{+0.25}_{-1.53}$	$1.45^{+0.07}_{-0.39}$	$2.28^{+0.11}_{-0.62}$
MACS J0025.4−1222	6.364154	−12.373026	0.586	…	…	LTM[i]	yes	$103.79^{+0.80}_{-1.50}$	$-0.84^{+0.02}_{-0.02}$	$16.73^{+0.40}_{-0.30}$	$2.02^{+0.05}_{-0.05}$	$2.37^{+0.06}_{-0.06}$
MACS J0035.4−2015	8.858893	−20.262288	0.352	$7.01^{+0.45}_{-0.50}$	$10.82^{+0.71}_{-0.79}$	L	yes	$146.91^{+3.57}_{-1.35}$	$-0.70^{+0.04}_{-0.03}$	$24.71^{+0.32}_{-0.17}$	$1.66^{+0.15}_{-0.06}$	$1.09^{+0.10}_{-0.04}$
						G	unknown	$174.08^{+28.47}_{-7.33}$	$-0.69^{+0.12}_{-0.11}$	$28.13^{+0.47}_{-0.78}$	$2.49^{+1.50}_{-0.84}$	$1.64^{+0.99}_{-0.55}$
MACS J0159.8−0849	29.955451	−8.832999	0.405	$7.20^{+0.61}_{-0.68}$	$11.17^{+0.97}_{-1.08}$	LTM[i]	no	$179.81^{+28.38}_{-5.00}$	$-1.12^{+0.13}_{-0.13}$	$30.97^{+1.47}_{-0.50}$	$1.90^{+0.75}_{-0.55}$	$1.50^{+0.59}_{-0.43}$
						G	unknown	$206.97^{+22.03}_{-26.62}$	$-0.71^{+0.01}_{-0.45}$	$33.31^{+0.47}_{-2.86}$	$3.12^{+0.59}_{-2.09}$	$2.44^{+0.46}_{-1.64}$
MACS J0257.1−2325	44.286469	−23.434684	0.5049	$6.22^{+0.70}_{-0.74}$	$9.69^{+1.12}_{-1.18}$	L	yes	$99.44^{+1.03}_{-11.95}$	$-0.96^{+0.01}_{-0.06}$	$16.01^{+0.09}_{-0.76}$	$0.53^{+0.01}_{-0.11}$	$0.54^{+0.01}_{-0.11}$
MACS J0308.9+2645	47.2331734	26.7605103	0.356	$10.76^{+0.63}_{-0.65}$	$16.79^{+1.01}_{-1.04}$	LTM[k]	no	$261.64^{+30.31}_{-2.03}$	$-0.87^{+0.04}_{-0.03}$	$46.59^{+1.15}_{-0.56}$	$4.99^{+0.98}_{-0.86}$	$3.34^{+0.66}_{-0.57}$
						G	unknown	$270.29^{+37.63}_{-16.50}$	$-0.68^{+0.08}_{-0.22}$	$47.31^{+2.25}_{-4.36}$	$5.45^{+2.27}_{-2.86}$	$3.63^{+1.51}_{-1.90}$
MACS J0417.5−1154	64.39454	−11.908851	0.443	$12.25^{+0.53}_{-0.55}$	$19.32^{+0.86}_{-0.89}$	L[l]	yes	$180.71^{+3.24}_{-2.81}$	$-0.59^{+0.02}_{-0.02}$	$37.35^{+0.36}_{-0.44}$	$3.10^{+0.16}_{-0.14}$	$2.71^{+0.14}_{-0.13}$

Table 1
(Continued)

Cluster	α J2000	δ J2000	$z_{\rm lens}$	M_{500} ($10^{14}M_\odot$)	M_{200} ($10^{14}M_\odot$)	Alg.	Spec-z	$M_{\rm SL}$(200kpc) ($10^{12}M_\odot$)	$S_{50–200}$	$e\theta_{\rm E}$ (arcsec)	$\mathcal{A}^{\rm lens}_{\|\mu\|\geqslant 3}$ (arcmin^2)	$\mathcal{A}^{0.5}_{\|\mu\|\geqslant 3}$ (arcmin^2)
MACS J0553.4−3342	88.330692	−33.707542	0.43	$8.77^{+0.44}_{-0.46}$	$13.70^{+0.70}_{-0.74}$	G[m]	yes	$190.98^{+0.65}_{-4.96}$	$-0.55^{+0.01}_{-0.02}$	$39.84^{+0.00}_{-1.42}$	$4.33^{+0.13}_{-0.27}$	$3.78^{+0.11}_{-0.23}$
						L	yes	$171.76^{+3.38}_{-4.61}$	$-0.41^{+0.03}_{-0.04}$	$42.30^{+0.15}_{-0.32}$	$4.53^{+0.26}_{-0.29}$	$3.83^{+0.22}_{-0.24}$
						G[m]	yes	$146.26^{+5.84}_{-4.52}$	$-0.56^{+0.05}_{-0.05}$	$41.06^{+0.73}_{-0.87}$	$3.39^{+0.43}_{-0.20}$	$2.86^{+0.36}_{-0.17}$
MS 1008.1−1224	152.634522	−12.664695	0.3062	$4.94^{+0.57}_{-0.60}$	$7.53^{+0.89}_{-0.93}$	L	yes	$130.62^{+5.46}_{-3.44}$	$-0.79^{+0.07}_{-0.06}$	$22.28^{+0.32}_{-0.91}$	$1.25^{+0.16}_{-0.13}$	$0.69^{+0.09}_{-0.07}$
PLCK G004.5−19.5[n]	289.270977	−33.522357	0.54	$10.36^{+0.68}_{-0.72}$	$16.40^{+1.10}_{-1.17}$	L	no	$244.86^{+24.94}_{-0.20}$	$-0.67^{+0.01}_{-0.01}$	$47.83^{+0.07}_{-0.17}$	$4.05^{+0.05}_{-0.02}$	$4.38^{+0.06}_{-0.02}$
PLCK G171.9−40.7	48.239437	8.369767	0.27	$10.71^{+0.49}_{-0.50}$	$16.58^{+0.78}_{-0.79}$	LTM[k]	no	$200.82^{+26.52}_{-2.64}$	$-0.90^{+0.06}_{-0.02}$	$40.57^{+1.36}_{-0.70}$	$2.58^{+0.61}_{-0.00}$	$1.18^{+0.28}_{-0.00}$
PLCK G287.0+32.9	177.709036	−28.082135	0.39	$14.69^{+0.39}_{-0.42}$	$23.17^{+0.63}_{-0.68}$	G	unknown	$229.52^{+22.95}_{-12.73}$	$-0.64^{+0.02}_{-0.14}$	$39.18^{+1.00}_{-1.29}$	$4.89^{+0.73}_{-1.79}$	$2.22^{+0.33}_{-0.81}$
						LTM[o]	no	$266.87^{+28.31}_{-2.93}$	$-0.68^{+0.05}_{-0.03}$	$53.84^{+0.64}_{-0.11}$	$8.19^{+0.97}_{-1.20}$	$6.15^{+0.73}_{-0.90}$
						G	unknown	$263.27^{+36.22}_{-0.08}$	$-0.40^{+0.02}_{-0.11}$	$55.68^{+2.25}_{-0.45}$	$9.72^{+0.77}_{-2.43}$	$7.27^{+0.58}_{-1.82}$
PSZ2 G209.79+10.23	110.598933	7.408627	0.677	$10.73^{+0.63}_{-0.66}$	$17.17^{+1.04}_{-1.08}$	L	yes	$108.11^{+10.91}_{-5.56}$	$-0.80^{+0.14}_{-0.08}$	$27.74^{+0.67}_{-0.88}$	$0.81^{+0.30}_{-0.15}$	$1.08^{+0.40}_{-0.21}$
RXC J0018.5+1626	4.639919	16.437871	0.546	$9.79^{+0.53}_{-0.53}$	$15.48^{+0.86}_{-0.86}$	L	yes	$182.29^{+3.38}_{-1.10}$	$-0.37^{+0.02}_{-0.02}$	$30.87^{+0.38}_{-0.48}$	$2.54^{+0.22}_{-0.02}$	$2.79^{+0.24}_{-0.02}$
RXC J0032.1+1808	8.049474	18.14366	0.3956	$7.61^{+0.57}_{-0.63}$	$11.81^{+0.91}_{-1.00}$	L	yes	$179.23^{+8.45}_{-0.82}$	$-0.65^{+0.09}_{-0.02}$	$50.11^{+0.62}_{-0.31}$	$6.51^{+0.82}_{-0.09}$	$4.98^{+0.63}_{-0.07}$
						LTM[p]	yes	$210.40^{+1.75}_{-1.07}$	$-0.57^{+0.02}_{-0.03}$	$49.67^{+0.31}_{-0.17}$	$7.47^{+0.04}_{-0.18}$	$5.71^{+0.03}_{-0.13}$
RXC J0142.9+4438	25.730087	44.634676	0.341	$9.02^{+0.60}_{-0.64}$	$14.00^{+0.95}_{-1.02}$	G	unknown	$199.67^{+30.38}_{-2.61}$	$-0.65^{+0.06}_{-0.02}$	$50.47^{+1.37}_{-0.29}$	$5.34^{+1.53}_{-0.70}$	$4.06^{+1.16}_{-0.53}$
						L[h]	no	$213.58^{+23.00}_{-2.46}$	$-0.71^{+0.03}_{-0.04}$	$34.15^{+0.17}_{-0.23}$	$3.10^{+0.58}_{-0.55}$	$1.96^{+0.37}_{-0.35}$
						G	unknown	$214.77^{+46.90}_{-11.71}$	$-0.66^{+0.03}_{-0.13}$	$34.31^{+0.36}_{-1.57}$	$3.68^{+1.31}_{-1.27}$	$2.32^{+0.82}_{-0.80}$
RXC J0232.2−4420	38.077317	−44.346666	0.2836	$7.54^{+0.33}_{-0.32}$	$11.59^{+0.52}_{-0.50}$	L	yes	$199.37^{+1.09}_{-6.63}$	$-0.69^{+0.03}_{-0.05}$	$30.50^{+0.11}_{-0.66}$	$2.76^{+0.08}_{-0.26}$	$1.36^{+0.04}_{-0.13}$
RXC J0600.1−2007	90.034008	−20.135751	0.46	$10.73^{+0.51}_{-0.54}$	$16.89^{+0.82}_{-0.87}$	L	no	$206.32^{+21.98}_{-9.74}$	$-0.37^{+0.02}_{-0.06}$	$39.99^{+0.72}_{-3.28}$	$3.67^{+0.48}_{-0.62}$	$3.35^{+0.44}_{-0.87}$
						G[m,q]	unknown	$218.82^{+47.28}_{-4.18}$	$-0.43^{+0.04}_{-0.05}$	$49.53^{+0.67}_{-0.00}$	$10.79^{+3.13}_{-2.93}$	$9.09^{+2.63}_{-2.47}$
RXC J0911.1+1746	137.797997	17.774794	0.5049	$6.99^{+0.73}_{-0.79}$	$10.92^{+1.17}_{-1.26}$	G	unknown	$112.81^{+68.38}_{-9.76}$	$-0.66^{+0.03}_{-0.34}$	$14.85^{+8.86}_{-0.57}$	$0.89^{+0.71}_{-0.35}$	$0.90^{+0.72}_{-0.35}$
RXC J0949.8+1707	147.4659	17.119601	0.3826	$8.24^{+0.46}_{-0.46}$	$12.80^{+0.73}_{-0.73}$	L	no	$159.34^{+38.42}_{-0.00}$	$-0.75^{+0.05}_{-0.05}$	$25.63^{+5.73}_{-0.00}$	$2.19^{+1.00}_{-0.00}$	$1.60^{+0.74}_{-0.00}$
						G	unknown	$181.02^{+43.57}_{-6.57}$	$-0.49^{+0.06}_{-0.08}$	$26.31^{+1.27}_{-0.51}$	$5.20^{+2.40}_{-1.39}$	$3.80^{+1.75}_{-1.01}$
RXC J2211.7−0350	332.941368	−3.828952	0.397	$10.50^{+0.50}_{-0.49}$	$16.43^{+0.80}_{-0.79}$	L[h]	yes	$295.64^{+1.89}_{-7.49}$	$-0.59^{+0.04}_{-0.11}$	$56.01^{+0.98}_{-2.67}$	$6.43^{+0.54}_{-1.15}$	$4.93^{+0.41}_{-0.88}$
						G	yes	$281.15^{+7.33}_{-16.63}$	$-0.77^{+0.07}_{-0.13}$	$51.30^{+2.08}_{-3.01}$	$4.53^{+1.15}_{-1.52}$	$3.47^{+0.88}_{-1.17}$
RXS J060313.4+4212−N	90.819495	42.244882	0.228	$10.76^{+0.45}_{-0.43}$	$16.60^{+0.71}_{-0.68}$	G	unknown	$153.09^{+48.68}_{-25.12}$	$-0.64^{+0.13}_{-0.23}$	$18.91^{+1.03}_{-1.57}$	$1.76^{+1.52}_{-0.81}$	$0.62^{+0.54}_{-0.29}$
RXS J060313.4+4212−S	90.851319	42.158696	0.228			G	unknown	$176.38^{+40.05}_{-26.50}$	$-0.71^{+0.03}_{-0.18}$	$26.55^{+0.58}_{-0.75}$	$2.33^{+0.45}_{-0.94}$	$0.83^{+0.16}_{-0.33}$
SMACS J0723.3−7327	110.826755	−73.454628	0.39	$8.39^{+0.33}_{-0.34}$	$13.05^{+0.53}_{-0.54}$	L	no	$136.36^{+25.68}_{-0.00}$	$-0.67^{+0.02}_{-0.09}$	$21.46^{+2.84}_{-0.00}$	$1.42^{+0.53}_{-0.21}$	$1.07^{+0.40}_{-0.16}$
						G	unknown	$157.22^{+36.19}_{-22.45}$	$-0.63^{+0.06}_{-0.19}$	$26.10^{+0.89}_{-2.60}$	$2.65^{+1.12}_{-1.29}$	$1.98^{+0.84}_{-0.96}$
SPT−CL J0615−5746	93.965434	−57.780113	0.972	$6.77^{+0.49}_{-0.54}$	$10.92^{+0.81}_{-0.89}$	L[r]	yes	$242.03^{+12.61}_{-11.26}$	$-0.54^{+0.04}_{-0.04}$	$34.45^{+2.69}_{-2.10}$	$2.47^{+0.33}_{-0.29}$	$4.19^{+0.56}_{-0.49}$
						LTM	yes	$233.74^{+3.49}_{-8.75}$	$-0.69^{+0.02}_{-0.06}$	$36.38^{+0.77}_{-1.58}$	$2.12^{+0.00}_{-0.09}$	$3.61^{+0.00}_{-0.15}$
SGAS[s]												
SDSS J0004−0103	1.216424	−1.0544069	0.514	$0.98^{+1.52}_{-0.73}$	$1.50^{+2.38}_{-1.13}$	L	yes	$40.82^{+5.85}_{-3.64}$	$-1.18^{+0.10}_{-0.05}$	$6.10^{+1.07}_{-0.88}$	$0.09^{+0.02}_{-0.02}$	$0.09^{+0.02}_{-0.02}$
SDSS J0108+0624	17.1751119	6.4121008	0.54778	…	…	L	yes	$88.36^{+0.07}_{-43.64}$	$-0.64^{+0.05}_{-0.18}$	$4.56^{+1.99}_{-1.64}$	$0.40^{+0.00}_{-0.35}$	$0.44^{+0.00}_{-0.39}$
SDSS J0146−0929	26.733363	−9.497921	0.4469	…	…	L	yes	$111.47^{+4.85}_{-4.24}$	$-0.98^{+0.04}_{-0.03}$	$16.20^{+0.31}_{-0.26}$	$0.65^{+0.07}_{-0.05}$	$0.57^{+0.06}_{-0.05}$
SDSS J0150+2725	27.503546	27.426761	0.30619	…	…	L	yes	$180.65^{+13.90}_{-3.64}$	$-0.52^{+0.07}_{-0.02}$	$19.64^{+3.01}_{-0.53}$	$2.82^{+0.78}_{-0.18}$	$1.54^{+0.43}_{-0.10}$
SDSS J0333−0651	53.269401	−6.856349	0.5729	…	…	L	yes	$81.42^{+11.68}_{-3.76}$	$-1.09^{+0.14}_{-0.01}$	$12.85^{+0.60}_{-0.46}$	$0.28^{+0.13}_{-0.03}$	$0.33^{+0.15}_{-0.04}$
SDSS J0851+3331	132.911942	33.518369	0.3689	$4.19^{+2.56}_{-1.83}$	$6.58^{+3.96}_{-2.88}$	L	yes	$160.28^{+3.44}_{-11.80}$	$-0.68^{+0.03}_{-0.09}$	$22.33^{+0.64}_{-1.38}$	$1.71^{+0.11}_{-0.33}$	$1.20^{+0.08}_{-0.23}$
SDSS J0915+3826	138.912799	38.449517	0.3961	$5.08^{+2.67}_{-1.97}$	$8.04^{+4.11}_{-3.09}$	L	yes	$131.77^{+10.21}_{-5.45}$	$-0.51^{+0.07}_{-0.06}$	$17.64^{+0.68}_{-0.31}$	$1.54^{+0.45}_{-0.25}$	$1.18^{+0.35}_{-0.19}$
SDSS J0928+2031	142.018891	20.52919	0.192	$5.89^{+5.71}_{-3.48}$	$9.23^{+8.91}_{-5.49}$	L	yes	$141.97^{+10.72}_{-10.55}$	$-0.83^{+0.05}_{-0.05}$	$13.14^{+0.44}_{-0.56}$	$1.37^{+0.23}_{-0.23}$	$0.37^{+0.06}_{-0.06}$
SDSS J0952+3434	148.167609	34.579473	0.357	$2.20^{+3.21}_{-1.63}$	$3.42^{+5.03}_{-2.56}$	L	yes	$103.35^{+7.84}_{-6.97}$	$-0.93^{+0.05}_{-0.06}$	$14.17^{+0.46}_{-0.19}$	$0.62^{+0.11}_{-0.09}$	$0.42^{+0.07}_{-0.06}$
SDSS J0957+0509	149.4132969	5.158845	0.448	$10.62^{+11.32}_{-6.49}$	$17.22^{+18.53}_{-10.61}$	L	yes	$58.18^{+2.54}_{-4.64}$	$-1.03^{+0.06}_{-0.03}$	$8.18^{+0.24}_{-0.48}$	$0.19^{+0.03}_{-0.02}$	$0.17^{+0.02}_{-0.02}$
SDSS J1038+4849	159.681586	48.821594	0.4308	$1.68^{+0.74}_{-0.56}$	$2.59^{+1.12}_{-0.84}$	L	yes	$70.65^{+2.20}_{-1.55}$	$-1.35^{+0.03}_{-0.01}$	$13.22^{+0.11}_{-0.12}$	$0.24^{+0.02}_{-0.01}$	$0.20^{+0.02}_{-0.01}$
SDSS J1050+0017	162.6663711	0.285224	0.5931	$0.93^{+0.57}_{-0.39}$	$1.44^{+0.87}_{-0.60}$	L	yes	$171.67^{+1.97}_{-1.59}$	$-0.55^{+0.03}_{-0.02}$	$23.73^{+0.17}_{-0.17}$	$1.92^{+0.15}_{-0.11}$	$2.27^{+0.17}_{-0.13}$
SDSS J1055+5547	163.769173	55.806467	0.466	$1.77^{+3.01}_{-1.34}$	$2.76^{+4.79}_{-2.10}$	L	yes	$165.78^{+3.00}_{-3.08}$	$-0.94^{+0.02}_{-0.03}$	$27.00^{+0.52}_{-0.53}$	$1.29^{+0.06}_{-0.07}$	$1.20^{+0.06}_{-0.07}$
SDSS J1110+6459	167.573863	64.996641	0.656	$5.21^{+5.07}_{-3.15}$	$8.45^{+8.22}_{-5.14}$	L	yes	$117.01^{+4.40}_{-7.38}$	$-0.61^{+0.04}_{-0.19}$	$16.22^{+0.80}_{-0.81}$	$0.55^{+0.03}_{-0.06}$	$0.71^{+0.03}_{-0.08}$
SDSS J1115+1645	168.7684547	16.7605789	0.537	…	…	L	yes	$93.38^{+6.93}_{-3.07}$	$-0.81^{+0.03}_{-0.03}$	$10.59^{+1.10}_{-0.40}$	$0.47^{+0.09}_{-0.04}$	$0.50^{+0.09}_{-0.05}$
SDSS J1138+2754	174.537311	27.908537	0.451	$21.69^{+23.51}_{-13.55}$	$36.00^{+38.98}_{-22.78}$	L	yes	$132.24^{+2.57}_{-3.42}$	$-0.77^{+0.03}_{-0.03}$	$20.78^{+0.20}_{-0.31}$	$1.10^{+0.04}_{-0.06}$	$0.98^{+0.04}_{-0.06}$
SDSS J1152+0930	178.19748	9.504093	0.517	$13.10^{+14.03}_{-8.07}$	$21.50^{+23.32}_{-13.35}$	L	yes	$156.56^{+0.55}_{-2.41}$	$-0.44^{+0.02}_{-0.02}$	$17.60^{+0.09}_{-0.33}$	$1.98^{+0.02}_{-0.08}$	$2.05^{+0.02}_{-0.08}$

Table 1

(Continued)

Cluster	α J2000	δ J2000	$z_{\rm lens}$	M_{500} ($10^{14}M_\odot$)	M_{200} ($10^{14}M_\odot$)	Alg.	Spec-z	$M_{\rm SL}$(200kpc) ($10^{12}M_\odot$)	$S_{50\text{–}200}$	$e\theta_{\rm E}$ (arcsec)	$\mathcal{A}^{\rm lens}_{\lvert\mu\rvert\geqslant 3}$ (arcmin^2)	$\mathcal{A}^{0.5}_{\lvert\mu\rvert\geqslant 3}$ (arcmin^2)
SDSS J1152+3313	178.000771	33.228271	0.3612	$3.10^{+1.44}_{-1.10}$	$4.81^{+2.20}_{-1.68}$	L	yes	$107.26^{+1.75}_{-0.06}$	$-0.79^{+0.02}_{-0.02}$	$11.18^{+0.08}_{-0.03}$	$0.67^{+0.03}_{-0.00}$	$0.46^{+0.02}_{-0.00}$
SDSS J1156+1911	179.02267	19.186919	0.54547	…	…	L	yes	$131.14^{+13.96}_{-40.05}$	$-0.69^{+0.06}_{-0.16}$	$14.68^{+2.76}_{-3.90}$	$1.01^{+0.29}_{-0.54}$	$1.10^{+0.31}_{-0.59}$
SDSS J1207+5254	181.899649	52.916438	0.275	$3.65^{+9.78}_{-3.29}$	$5.70^{+15.72}_{-5.16}$	L	yes	$108.72^{+15.07}_{-17.54}$	$-0.77^{+0.08}_{-0.06}$	$9.16^{+0.80}_{-0.39}$	$0.73^{+0.31}_{-0.22}$	$0.34^{+0.15}_{-0.10}$
SDSS J1209+2640	182.348771	26.679503	0.5606	$7.85^{+6.62}_{-4.16}$	$12.73^{+10.80}_{-6.79}$	L	yes	$208.00^{+1.13}_{-0.36}$	$-0.76^{+0.02}_{-0.02}$	$32.35^{+0.22}_{-0.10}$	$2.23^{+0.02}_{-0.03}$	$2.51^{+0.02}_{-0.03}$
SDSS J1329+2243	202.39391	22.721064	0.4427	$3.26^{+2.03}_{-1.43}$	$5.12^{+3.15}_{-2.24}$	L	yes	$128.87^{+1.47}_{-13.96}$	$-0.54^{+0.02}_{-0.11}$	$10.75^{+0.14}_{-0.27}$	$1.42^{+0.04}_{-0.44}$	$1.24^{+0.04}_{-0.38}$
SDSS J1336−0331	204.00035	−3.524963	0.17637	…	…	L	yes	$162.81^{+5.45}_{-12.07}$	$-0.77^{+0.04}_{-0.03}$	$15.26^{+0.39}_{-1.05}$	$1.86^{+0.16}_{-0.31}$	$0.45^{+0.04}_{-0.08}$
SDSS J1343+4155	205.886851	41.917627	0.418	$5.88^{+7.94}_{-4.15}$	$9.34^{+12.78}_{-6.65}$	L	yes	$159.73^{+3.76}_{-27.96}$	$-0.39^{+0.02}_{-0.09}$	$16.96^{+0.45}_{-2.37}$	$2.42^{+0.12}_{-0.84}$	$1.98^{+0.10}_{-0.68}$
SDSS J1420+3955	215.166797	39.918593	0.607	$6.55^{+4.42}_{-3.09}$	$10.61^{+7.11}_{-4.96}$	L	yes	$186.56^{+1.52}_{-3.04}$	$-0.59^{+0.03}_{-0.02}$	$29.87^{+0.30}_{-0.62}$	$3.69^{+0.19}_{-0.19}$	$4.47^{+0.23}_{-0.23}$
SDSS J1439+1208	219.790757	12.140434	0.42734	…	…	L	yes	$209.01^{+4.56}_{-4.78}$	$-0.38^{+0.03}_{-0.03}$	$32.09^{+1.65}_{-1.61}$	$4.35^{+0.43}_{-0.38}$	$3.65^{+0.36}_{-0.32}$
SDSS J1456+5702	224.003682	57.03898	0.484	$18.93^{+17.94}_{-10.91}$	$31.14^{+29.87}_{-18.04}$	L	yes	$123.23^{+2.10}_{-10.24}$	$-0.94^{+0.02}_{-0.07}$	$17.62^{+0.13}_{-0.68}$	$0.78^{+0.04}_{-0.16}$	$0.75^{+0.04}_{-0.15}$
SDSS J1522+2535	230.719852	25.590965	0.602	$8.38^{+9.92}_{-5.52}$	$13.70^{+16.52}_{-9.12}$	L	yes	$202.27^{+8.28}_{-12.03}$	$-0.39^{+0.05}_{-0.07}$	$30.90^{+2.09}_{-3.54}$	$3.36^{+0.44}_{-0.75}$	$4.04^{+0.52}_{-0.90}$
SDSS J1531+3414	232.79429	34.240312	0.335	$5.91^{+4.99}_{-3.14}$	$9.36^{+7.91}_{-4.99}$	L	yes	$127.39^{+15.83}_{-0.47}$	$-0.84^{+0.10}_{-0.02}$	$20.71^{+2.52}_{-0.24}$	$1.09^{+0.42}_{-0.03}$	$0.68^{+0.26}_{-0.02}$
SDSS J1604+2244	241.042271	22.738579	0.286	$6.92^{+11.38}_{-5.26}$	$10.95^{+18.28}_{-8.41}$	L	yes	$70.92^{+23.60}_{-3.64}$	$-1.13^{+0.09}_{-0.05}$	$12.57^{+3.71}_{-0.00}$	$0.31^{+0.22}_{-0.02}$	$0.15^{+0.11}_{-0.01}$
SDSS J1621+0607	245.384938	6.121973	0.3429	$2.30^{+1.32}_{-0.94}$	$3.55^{+2.01}_{-1.44}$	L	yes	$139.79^{+1.38}_{-3.55}$	$-0.73^{+0.02}_{-0.02}$	$16.12^{+0.13}_{-0.49}$	$1.30^{+0.03}_{-0.08}$	$0.83^{+0.02}_{-0.05}$
SDSS J1632+3500	248.042757	35.008267	0.466	$9.53^{+13.46}_{-6.73}$	$15.46^{+22.31}_{-11.04}$	L	yes	$166.03^{+3.78}_{-45.46}$	$-0.55^{+0.02}_{-0.23}$	$22.82^{+0.69}_{-6.05}$	$2.02^{+0.13}_{-1.12}$	$1.87^{+0.12}_{-1.04}$
SDSS J1723+3411	260.90068	34.199481	0.44227	…	…	L	yes	$80.21^{+10.24}_{-2.88}$	$-0.93^{+0.14}_{-0.04}$	$9.59^{+0.41}_{-0.22}$	$0.34^{+0.11}_{-0.03}$	$0.30^{+0.14}_{-0.01}$
SDSS J2111−0114	317.830623	−1.239844	0.6363	$6.42^{+3.55}_{-2.68}$	$10.40^{+5.69}_{-4.30}$	L	yes	$155.66^{+5.98}_{-17.94}$	$-0.50^{+0.05}_{-0.16}$	$18.39^{+0.36}_{-6.37}$	$1.63^{+0.21}_{-0.53}$	$2.07^{+0.27}_{-0.67}$
SDSS J2243−0935	340.836359	−9.588595	0.447	$5.53^{+4.99}_{-3.10}$	$8.81^{+8.04}_{-4.97}$	L	yes	$214.79^{+0.62}_{-1.06}$	$-0.27^{+0.01}_{-0.01}$	$42.60^{+0.38}_{-0.39}$	$8.19^{+0.19}_{-0.23}$	$7.23^{+0.17}_{-0.20}$

Notes. α and δ refer to the R.A. and decl. of the brightest cluster galaxy (BCG) selected in the analysis. $z_{\rm lens}$ refers to the redshift of the cluster. M_{500} and M_{200} are the large-scale mass estimates, measured independent of the lensing analyses. Alg. refers to the modeling algorithm used: L = `Lenstool`, LTM = Light-Traces-Mass, G = GLAFIC, GL = GRAVLENS, and GR = GRALE. For the HFF `Lenstool` models, letters after the dash indicate the lens-modeling team, where L-S = Sharon, L-CATS = CATS, and L-Cam = Caminha. Spec-z indicates whether the lens model employs a spectroscopic redshift constraint or if it is unknown whether a spectroscopic constraint is used. $M_{\rm SL}$(200kpc) refers to the mass within a 200 kpc aperture from the BCG, computed from the strong lens model. $S_{50\text{–}200}$ refers to the logarithmic slope of the projected mass-density profile in the range of 50–200 kpc from the BCG. $e\theta_{\rm E}$ is the effective Einstein radius for $z_s = 9$. $\mathcal{A}^{\rm lens}_{\lvert\mu\rvert\geqslant 3}$ is the noncorrected lensing strength and $\mathcal{A}^{0.5}_{\lvert\mu\rvert\geqslant 3}$ is the distance-corrected lensing strength for $z_s = 9$. The availability of lensing constraints in the GLAFIC models of RELICS clusters is based on Table A1 of Okabe et al. (2020). This table is available at the Strasbourg astronomical Data Center (CDS) via anonymous ftp to cdsarc.u-strasbg.fr (130.79.128.5) or via https://cdsarc.unistra.fr/viz-bin/cat/J/ApJ/928/87.

[a] HFF model references: Johnson et al. (2014);

[b] Kawamata et al. (2018);

[c] Raney et al. (2020a);

[d] Lagattuta et al. (2019);

[e] Caminha et al. (2017);

[f] Lagattuta et al. (2019);

[g] Abell 1758a has two major components (northwest and southeast). Although contained in one model, the amplification areas of the lensing strength we compute (see Section 3.1) for each component do not intersect. We therefore split the model into northwest and southeast components. RXS J060313.4+4212 has a northern and southern component, modeled separately. Because they have been separated into components, we do not include the Planck SZ M_{500} mass of these two clusters in total mass comparisons.

[h] RELICS model references: Cerny et al. (2018);

[i] Cibirka et al. (2018);

[j] Acebron et al. (2019);

[k] Acebron et al. (2018);

[l] Mahler et al. (2019);

[m] Denotes the three GLAFIC models in which an additional 5% was added to the upper error bar of the lensing strength to account for the magnification map not including the entire $\lvert\mu\rvert \geqslant 3$ region.

[n] PLCK G004.5−19.5 lens redshift was updated to $z = 0.519$ in Albert et al. (2017). The cluster lens was modeled at the redshift reported in the table.

[o] Zitrin et al. (2017);

[p] Acebron et al. (2020);

[q] The GLAFIC model of RXC J0600.1−2007 employs an updated redshift of 0.43 from more recent spectroscopy with the Multi Unit Spectroscopic Explorer on the Very Large Telescope.

[r] Paterno-Mahler et al. (2018);

[s] SGAS model reference: Sharon et al. (2020).

publicly available to the community on MAST[2]. Not all the lines of sight in the RELICS program resulted in successful lens models. This is primarily due to the lack of identified lensing constraints in some of the clusters. RELICS models are typically based on a handful of lensed galaxies—compared with hundreds for HFF. This may result in underconstrained models (e.g., Cerny et al. 2018). We include in our analysis all publicly available models that were either published or satisfy the following criteria: the model-predicted lensed images are consistent with the observed lensing evidence to within $1\farcs5$, and the model does not produce major mass components or critical curves that protrude into regions with no constraints or a physical motivation. This resulted in all the available `Lenstool` models (22), all the available LTM models (10), and most of the GLAFIC models (21). Several clusters were modeled by more than one method, which helps in indicating systematic uncertainties that are due to modeling approaches. However, it is beyond the scope of this paper to conduct a thorough investigation of the differences that may exist between different models of the same cluster. Some examples of these comparisons between the different RELICS lens models can be found in Acebron et al. (2019, 2020).

Three of the GLAFIC lens models did not have a large enough field of view to capture all the area of moderate magnification, $|\mu| \geqslant 3$, which is required for our analysis (see Section 3.1). For these models, we report the measured value, but add an additional 5% to the upper error bar, based on a power-law extrapolation of the best model magnification maps. We mark these models in Table 1 and indicate them with a dashed black border in plots including lensing strength. Lastly, Abell 1758a has two major components (northwest and southeast). Although contained in one model, the amplification areas of the lensing strength we compute (see Section 3.1) for each component do not intersect. We therefore split the model into northwest and southeast components.

2.3. SGAS

The science goal of the Sloan Giant Arcs Survey (SGAS, Sharon et al. 2020) is to study the star formation history and physical properties of highly magnified galaxies at cosmic noon ($1 \gtrsim z \gtrsim 3$), using the magnification of strong-lensing clusters to both amplify the light from these galaxies and resolve individual star-forming regions. The SGAS clusters were selected from the Sloan Digital Sky Survey (SDSS; Blanton et al. 2017) based on the identification of strong-lensing evidence (Bayliss et al. 2011; Sharon et al. 2020). This sample extends to lower cluster masses than RELICS and HFF. We use 35 public `Lenstool` models of SGAS clusters from Sharon et al. (2020), excluding SDSS J1002+2031 and SDSS J1527+0652, which were categorized by Sharon et al. (2020) as being too poorly constrained (see Sharon et al. 2020 for more details).

3. Methods

In this section, we define the lensing-strength indicator ($\mathcal{A}^{0.5}_{|\mu|\geqslant 3}$) and the three cluster properties investigated in this work as predictors of lensing strength: large-scale mass (M_{500}), strong-lensing projected core mass ($M_{\mathrm{SL,\,core}}$), and the inner slope (S_{50-200}) of the projected mass-density profile. We also determine the effective Einstein radius ($e\theta_E$), often used to judge lensing strength, for comparison with these other cluster properties and our lensing-strength indicator. Lastly, for SGAS clusters and suitable RELICS and HFF clusters, we measure the distance between the brightest cluster galaxy (BCG) and the farthest bright arc, a common indicator of lensing strength from imaging data without a lens model, to compare with our lensing-strength measurement.

Each publicly available lens model was provided with a range of mass maps that sample the posterior probability distribution of the lens model, usually $\sim$100 maps, for computing uncertainties. For all quantities we compute from the lens models, statistical uncertainties are given as the interval that contains 68% of the values computed from these "range" models.

3.1. Lensing Strength

The magnification (μ) of a point in the image plane is the factor by which a source is magnified as a result of its light passing through the lens plane. The magnification is defined as follows,

$$\mu \equiv ((1-\kappa)^2 - \gamma^2)^{-1}, \tag{1}$$

where κ and γ are the convergence and shear of the lensing potential, respectively.

Several authors have used a definition of "lensing strength" as the image-plane area in which a source at redshift z_s is magnified by a factor μ or above (e.g., Richard et al. 2014; Grillo et al. 2015; Caminha et al. 2017; Cerny et al. 2018; Coe et al. 2019, and references therein). In this paper, we focus our analysis on $z_s = 9$ and $|\mu| \geqslant 3$. We define the lensing strength of a cluster as the area in the image plane where a source at redshift 9 is magnified by at least a factor of 3, denoted as $\mathcal{A}^{\mathrm{lens}}_{|\mu|\geqslant 3}$. A threshold of $|\mu| \geqslant 3$ allows for significant magnification, which is important for studies of the background universe, and remains close enough to the strong-lensing core, where the constraints are. Additionally, the uncertainty in the overall magnification of a lens is dominated by the inaccuracy in regions of high magnification ($|\mu| > 10$) or high length-to-width[3] ratios ($\mathrm{l/w} > 10$), which was demonstrated in several studies (e.g., Giocoli et al. 2012; Cerny et al. 2018; Raney et al. 2020b).

A source redshift of $z_s = 9$ is chosen in order to home our investigation in on the applicability for discovery of high-redshift galaxies, as this is the typical redshift sought by lensing-assisted high-z searches (e.g., RELICS, HFF). Moreover, for sources beyond $z_s \sim 6$, the magnification map does not change considerably.

Finally, we normalize $\mathcal{A}^{\mathrm{lens}}_{|\mu|\geqslant 3}$ to a lens redshift of $z = 0.5$, by multiplying it by the ratio of the angular diameter distances squared, to account for the geometric dependence of the area on the distance to the lens.

$$\mathcal{A}^{0.5}_{|\mu|\geqslant 3} \equiv \mathcal{A}^{\mathrm{lens}}_{|\mu|\geqslant 3}\left(\frac{D_L}{D_{0.5}}\right)^2 \tag{2}$$

where $\mathcal{A}^{0.5}_{|\mu|\geqslant 3}$ is the lensing strength normalized to $z = 0.5$, D_L is the angular diameter distance from the observer to the lens,

---

[2] https://doi.org/10.17909/T9SP45

[3] The length-to-width ratio for large arcs is proportional to the magnification μ for similar convergence κ and can be approximated as $L/W \simeq \lambda_2/\lambda_1 \simeq 4\mu(1-\kappa)^2$ (Bartelmann & Weiss 1994).

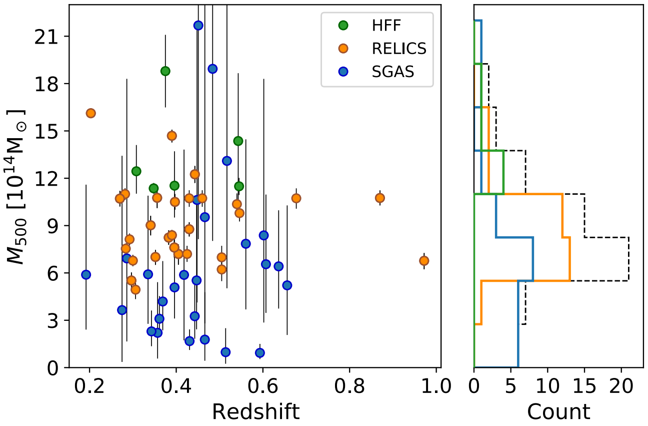

Figure 1. The mass vs. redshift distribution of the clusters included in this work, separated by the three surveys from which the sample was assembled. See Section 3.2 for a description of the M_{500} estimates, which are measured independent of the lensing analyses.

and $D_{0.5}$ is the angular diameter distance from the observer to $z = 0.5$.

In Table 1, we list the nonnormalized lensing strength ($\mathcal{A}^{\rm lens}_{|\mu|\geqslant 3}$) as well as the normalized lensing strength ($\mathcal{A}^{0.5}_{|\mu|\geqslant 3}$). Figure 2 shows the distribution of normalized lensing strengths across the sample of clusters. In Figure 2, `Lenstool` models are used where available (using the Sharon models for the HFF clusters), LTM if there is no `Lenstool` model, and GLAFIC if there is no `Lenstool` or LTM model.

The availability of spectroscopic constraints has a significant impact on the magnification uncertainty of a lens model. For example, by analyzing lens models of simulated clusters with and without spectroscopic constraints, Johnson & Sharon (2016) found that models with no spectroscopic redshift constraints have the highest magnification uncertainties, up to ∼ 10%. This can clearly affect the lensing-strength quantity we measure in a nontrivial way. While all the HFF and SGAS models rely on spectroscopic redshift constraints, 29 of the RELICS models of 19 clusters do not (see Table 1). We evaluate a conservative estimate of the extra uncertainty introduced to the computed lensing strength due to the lack of spectroscopic information, as follows. First, we increase by 10% the magnification maps of the range models that have a lensing strength above the best model value, and reduce by 10% those with a lensing strength below the best model value. We then recompute the 68% confidence interval from the modified maps, keeping the best model unmodified. Treating the models with a lensing strength above or below the best model separately prevents any from crossing over, such as a model with a lensing strength originally below the best model that would surpass it with the 10% boost. This keeps the error bar more conservative, as models crossing over could reduce the 68% confidence interval. Overall, this boosts both sides of the error bar to conservatively account for the nontrivial dependence of the lensing strength on a 10% uncertainty in the magnification map. In Figures 4–6, red error bars indicate models without spectroscopic redshift constraints or if it is unknown whether a spectroscopic constraint is used.

We focus our analysis on the normalized lensing strength, but show comparisons with the nonnormalized lensing strength in the Appendix. We note that the conclusions of this work are independent of this choice.

3.2. Large-scale Mass Estimates

Large-scale mass proxies have been used to predict lensing strength in survey design (e.g., LoCuSS, Smith et al. 2005; RELICS, Coe et al. 2019). To test how well lensing strength correlates with total mass, we have obtained a large-scale mass estimate, reaching beyond the strong-lensing regime, for as many clusters in our sample as possible. For clusters included in the RELICS survey, we use the Planck SZ M_{500} mass (Table 1). MACS J0025.4−12 and CL J0152.7−1357 do not have a Planck SZ mass and thus are not included in this comparison. Furthermore, Abell 1758a, RXS J060313.4+4212-N, and RXS J060313.4+4212-S are not included in this comparison because the northern and southern components of RXS J060313.4+4212 were modeled separately; similarly, we split the Abell 1758a model into northwest and southwest components, as described in Section 2.2.

HFF clusters Abell S1063 and MACS J0717.5+3745 are included in the Planck SZ catalog (Planck Collaboration et al. 2016), providing a M_{500} estimate. For Abell 370, we use the M_{500} estimate reported in Umetsu et al. (2011). X-ray temperatures for MACS J1149.5+2223 and MACS J0416.1−2403 were reported by Postman et al. (2012) and for Abell 2744 by Allen (1998). We convert the X-ray temperature to M_{500} using the empirical relation from Arnaud et al. (2007).

For the SGAS clusters, we apply well-established methods in the literature to derive M_{500} estimates from the velocity dispersion measurements reported by Sharon et al. (2020), as described below. The velocity dispersions reported by Sharon et al. (2020) were derived for each cluster from cluster members with spectroscopic redshifts ($N_{\rm spec} \geqslant 4$), using the Gapper and bi-weight methods (Beers et al. 1990). In order to derive M_{500} estimates from the velocity dispersions in Sharon et al. 2020, we follow four steps. (1) We first convert the velocity dispersion to M_{200} using the $\sigma_{\rm DM} - M_{200}$ relation from Evrard et al. (2008), assuming a velocity bias $b_v = \sigma_g/\sigma_{\rm DM} = 1$, following Bayliss et al. (2011, and references therein). The resulting M_{200} values are consistent with those calculated by Sharon et al. 2020, who used the same method. (2) We derive the concentration c_{200} and its uncertainty using the concentration-mass relation reported by Child et al. (2018) for individual halos. (3) From a normal distribution of c_{200} concentrations, we randomly select 10,000 c_{200} values and compute the corresponding c_{500} for each using Appendix C of Hu & Kravtsov (2003), taking r_{200} as the virial radius. (4) Finally, we use c_{200} and c_{500} to convert M_{200} to M_{500}, following Hu & Kravtsov (2003). From the final distribution of M_{500} values of each cluster, we take the median as the M_{500} estimate. The statistical uncertainty is estimated by determining where 68% of the M_{500} values on either side of the median are included.

We note that the velocity dispersions computed for some SGAS clusters rely on a small number of galaxy redshifts. Seven SGAS clusters have 10 or fewer galaxy redshift measurements included in their velocity dispersion calculations. For velocity dispersions computed by Sharon et al. (2020), the uncertainty is given by the empirical relation reported by Ruel et al. (2014), which depends on the number of galaxy redshifts. In our method for estimating M_{500} from the velocity dispersion, we propagate these uncertainties. For velocity dispersions listed but not computed by Sharon et al. (2020) (five of the clusters with 10 or fewer galaxy redshifts), we acknowledge that the empirical formula reported by Ruel et al. (2014) would suggest slightly larger uncertainties. The

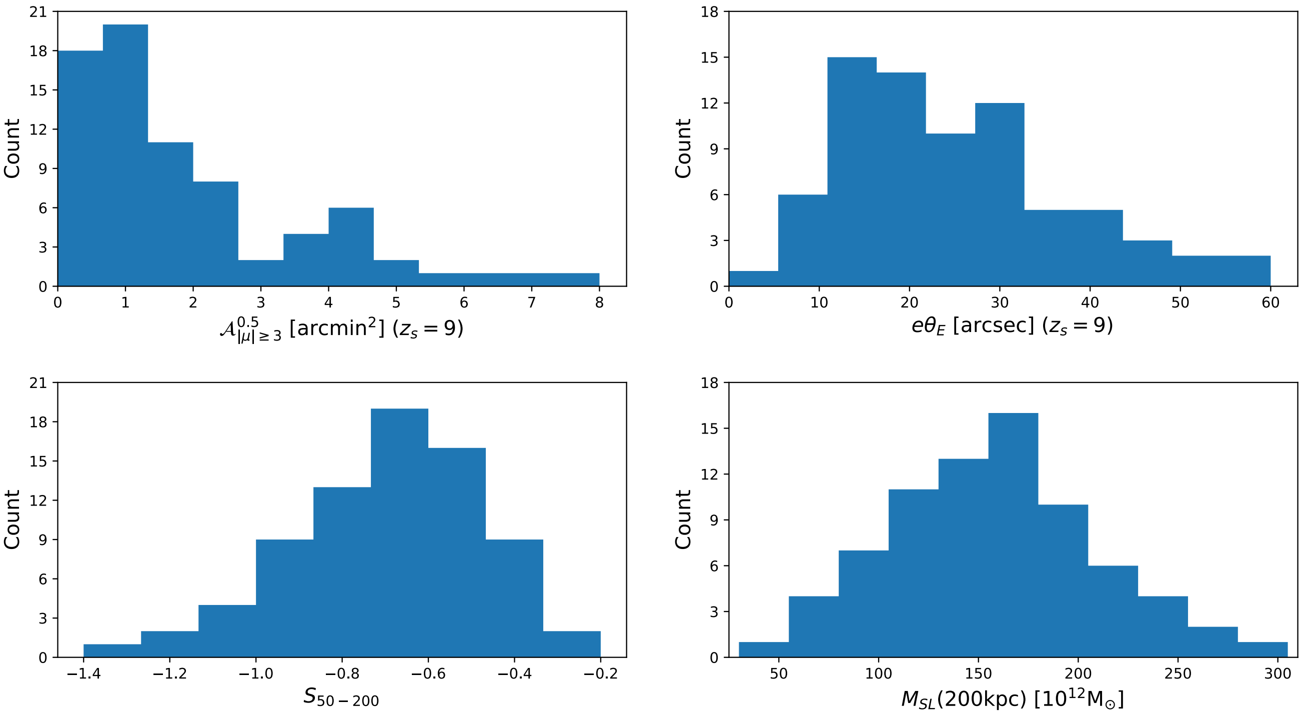

Figure 2. Distribution of cluster properties computed from the strong-lensing models. *Top left*: Normalized lensing strength, defined as the image-plane area with $|\mu| \geqslant 3$ for $z_s = 9$ and corrected for the redshift dependence of area projection onto the sky. *Top right*: Effective Einstein radius for $z_s = 9$. *Bottom left*: Slope of the projected mass-density profile, measured between 50 and 200 kpc from the BCG. *Bottom right*: Core mass, defined as the projected mass within 200 kpc of the BCG. `Lenstool` models are used where available (using the Sharon models for the HFF clusters), LTM if there is no `Lenstool` model, and GLAFIC if there is no `Lenstool` or LTM model.

uncertainty of the M_{500} estimate we compute for these clusters may therefore be underestimated. We refer the reader to Sharon et al. (2020) for specifics about these clusters. We emphasize that our study relies on the entire sample. We do not require very accurate M_{500} estimates for each individual cluster, only a good estimate to help identify trends across a large sample. Studies including Ruel et al. (2014) and Beers et al. (1990) report that these velocity dispersion estimators are unbiased, and we find no indication of a particular bias that would lead to our M_{500} estimates of clusters, with only a few galaxy redshifts being systematically biased low or high. We therefore contend that our reported uncertainties encompass the uncertainty introduced by having few galaxy redshifts, with the possible exception of the few clusters with potentially underestimated uncertainties. Furthermore, inaccuracies in M_{500} estimates of clusters based on few galaxy redshifts simply boost the scatter in the trends we investigate, rather than adding a particular bias.

Figure 1 displays the distribution of M_{500} estimates across the sample. Table 1 contains the corresponding values. We focus our analysis on M_{500}, but show comparisons with M_{200} in the Appendix.

3.3. Projected Core Mass Estimates from Strong Lensing

Strong-lensing models provide a detailed description of the mass distribution in the cores of galaxy clusters. We use the projected mass-density maps that were derived from the strong-lensing models of each cluster; these maps include cluster scale and galaxy scale halos. We obtain a cylindrical core mass measurement, $M_{\rm SL}$(200kpc), by summing the projected mass density within a 200 kpc aperture centered on the BCG, which is selected by visual inspection. In a few cases, such as where there are two or more galaxies with comparable brightnesses, we select the central bright galaxy that is more consistent with the center of the primary lensing potential as determined from the distribution of the lensing evidence.

The availability of spectroscopic redshift constraints (Section 3.1) also affects the accuracy of mass estimates derived from strong lens models. In a detailed study of the CLASH and HFF cluster, RXC J2248.7−4431 (Abell S1063), Caminha et al. (2016) find that lack of information on the source redshift of lensed constraints leads to model-predicted source redshifts biased toward higher values. The derived cluster mass is thus biased toward lower values, due to the degeneracy between total cluster mass and source redshift. They conclude that the impact on the total mass is not very significant, but quantities dependent on cosmological distances would be greatly affected. In a study of simulated clusters, Johnson & Sharon (2016) find that models with no spectroscopic constraints are biased toward lower masses by 5%-10%. Furthermore, Remolina González et al. (2021) find the mass within the effective Einstein radius to be biased low by 7.22% without a known background source redshift, using Single-Halo models of clusters in the "Outer Rim" simulation (Heitmann et al. 2019). The 4% bias found by Caminha et al. (2016) for Abell S1063 is within with these findings. To conservatively account for the bias found in these studies, for the models in our sample with no spectroscopic constraints we add a systematic uncertainty of $0.1 \times M_{\rm SL}$(200kpc) to the upper error bar of $M_{\rm SL}$(200kpc).

A correlation between the lensing strength and the mass enclosed in the core is expected, from the basic equations of gravitational lensing. For example, the Einstein radius for a spherically symmetric lens is proportional to the square root of the mass enclosed within it (see also Section 4.4). Figure 2 displays the distribution of core masses across the sample of

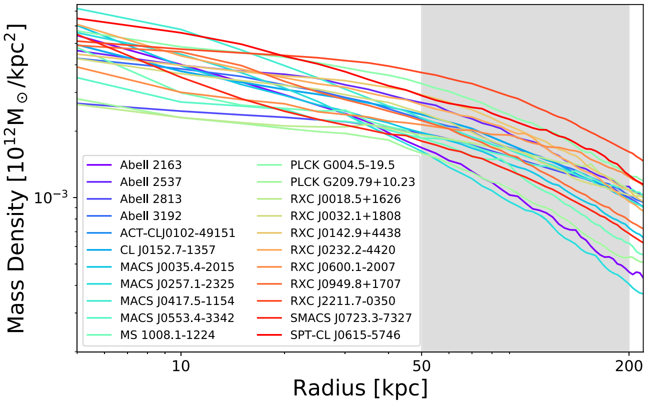

Figure 3. Projected mass-density profiles of `Lenstool` models for clusters of the sample included in the RELICS program. The gray shaded region indicates where the slope is measured (S_{50-200}). Clusters show clear differences in their projected density distributions in this region.

clusters. Table 1 contains the corresponding core masses for each cluster, as obtained from each modeling method.

3.4. Inner Slope of Projected Mass-density Profile

The third cluster property we investigate is the steepness of the projected mass-density profile at the core, extending the analysis beyond lensing-strength indicators that are based purely on total mass. The inner slope is measured from the strong-lensing mass maps.

As was done in Section 3.3, we use the total projected mass-density maps, which include both the cluster scale and galaxy scale components. This allows the profile to reflect physical cluster properties such as substructure, multiple major mass components, and stellar mass. Using the total mass map also helps minimize the degeneracies between the different components of the strong-lensing model.

The projected density profile is computed from the average densities inside concentric annuli, centered on the chosen BCG, in steps of 5 kpc. As an illustration of the range of projected mass profiles, Figure 3 shows the projected mass-density profiles computed for clusters included in the RELICS sample and modeled with `Lenstool`. We measure the logarithmic slope between 50 kpc and 200 kpc by fitting the average density profile with a power law using curve_fit in the Python module scipy.optimize[4]. We denote the slope as S_{50-200}.

The motivation for measuring the slope at projected radii larger than 50 kpc is to avoid the region typically dominated by the BCG, and to be less sensitive to a possible offset between the BCG and the dark matter (DM) halo. During the modeling procedure, the center of the main dark matter halo is usually allowed to vary. Unless constrained by lensing features at the very center of the cluster (typically radial arcs), the offset between the center of the main dark matter halo and the BCG is not well constrained. Harvey et al. (2017) explored the BCG offset of 10 dynamically relaxed clusters, and found that the BCG wobbles with an amplitude of $11.82^{+7.3}_{-3.0}$ kpc with respect to the centroid of the DM halo, assuming it can be described as a harmonic oscillator. Harvey et al. (2019) investigated the median BCG offset for different dark matter cross sections using the BAryons and HAloes of MAssive Systems simulations (BAHAMAS; McCarthy et al. 2017) and found the median offset to be below 10 kpc, lowest for dark matter with no cross section. Taking 50 kpc as the inner boundary of the slope measurement range allows us to mitigate this uncertainty. Furthermore, most of the light of BCGs lies within 50 kpc, indicating that most of their stellar mass would be enclosed in this range too.

We note that some studies have used normalized profiles (e.g., Bonamigo et al. 2018 and Caminha et al. 2019 scale the projected mass density by $\pi r_{200c}^2/M_{200c}$ and the radius by $1/r_{200c}$), which may simplify comparisons between clusters. We refrain from using a similar normalization here, in order to avoid introducing the large uncertainties on M_{200c} and r_{200c} into measurements at small projected radii. The estimated statistical uncertainty of the slope measurement takes into account both the range of slopes across the "range" mass maps that were provided with each of the public models (i.e., lens-modeling uncertainty) and the uncertainty associated with fitting the slope to the mass map. The former samples the posterior probability distribution in the mass distribution related to the modeling process to assess the degree of uncertainty in the slope estimate; the latter assesses the uncertainty of the slope fitted to the best model in the region 50–200 kpc from the BCG. We add these statistical uncertainties in quadrature.

For the GLAFIC lens models of clusters included in the RELICS program, a linear interpolation is applied to increase the map resolution of the "range" models from 0.4 to $0\overset{''}{.}05$ pixel^{-1}. This is necessary to accommodate the 5 kpc step size, enabling a smooth profile that is not significantly affected by pixel size. The interpolated maps are used throughout our analysis. Table 1 contains the slope (S_{50-200}) for each cluster and modeling method. The bottom left panel of Figure 2 displays the distribution of slopes across the sample.

3.5. Effective Einstein Radius and Area

The fourth property we explore is the effective Einstein radius ($e\theta_{\rm E}$), defined as the radius of a circle with an area the same as the area enclosed by the main tangential critical curve. The tangential critical curve is the theoretical line of infinite magnification; its naming indicates the primary direction in which the images (arcs) are magnified. To determine the tangential critical curve from the strong-lensing models, we compute the inverse of the magnification in the tangential direction, $\mu_t^{-1} = 1 - \kappa - \gamma$, for a background source redshift at $z_s = 9$. Table 1 contains the effective Einstein radius for each cluster and modeling method for $z_s = 9$. The top right panel of Figure 2 shows the distribution of effective Einstein radii across the sample. In order to compare with the lensing-strength area, we use the area within the main tangential critical curve (effective Einstein area, $\pi\theta_{\rm E}^2$).

The effective Einstein area is expected to have a strong correlation with our definition of lensing strength. In the bottom left panel of Figure 4, we compare $\mathcal{A}^{0.5}_{|\mu|\geqslant 3}$ with $\pi\theta_{\rm E}^2$ for each field. We also plot the expected relationship for three different potentials, at $z_{\rm lens} = 0.5$ and no ellipticity. Maroon shows a singular isothermal sphere (SIS). Blue shows a pseudoisothermal elliptical mass distribution (PIEMD; Kassiola & Kovner 1993) with a core radius of 40 kpc and a cut radius of 1500 kpc. Purple shows an NFW (Navarro et al. 1997) distribution with a scale radius of 100 kpc. The curves are created by varying the mass of the halo, keeping the core and cut radii constant in the PIEMD case and keeping the scale radius constant in the NFW case. In the SIS model, the two are related by a constant factor. In the

---

[4] Python scipy.optimize https://docs.scipy.org/doc/scipy/reference/tutorial/optimize.html

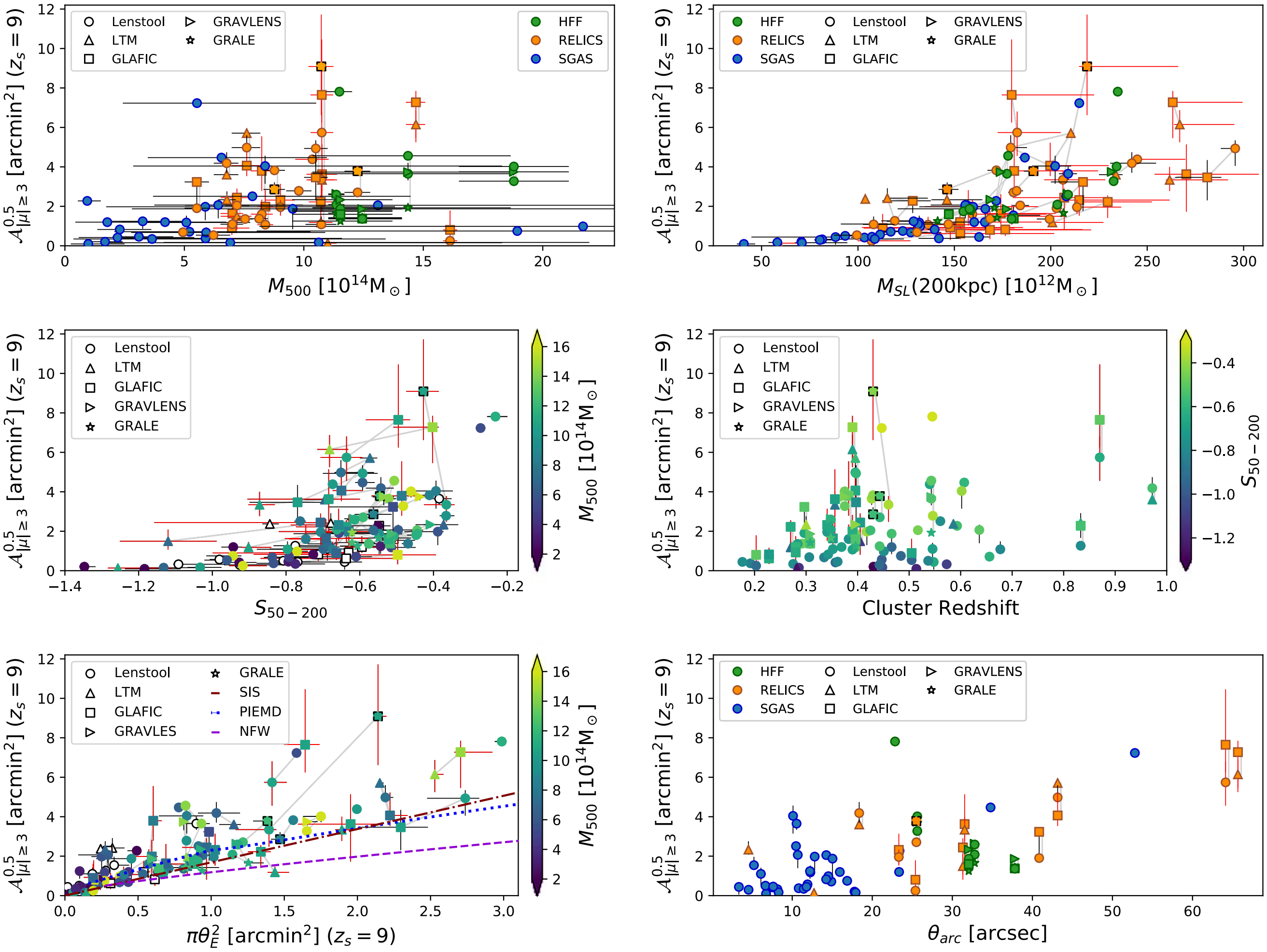

Figure 4. Normalized lensing strength ($\mathcal{A}^{0.5}_{|\mu|\geqslant 3}$) compared with cluster properties. *Top left:* Large-scale mass estimate (M_{500}), which is measured independently of the lensing analyses. *Top right:* Projected mass within 200 kpc of the BCG ($M_{\rm SL}$(200kpc)). *Middle left:* Inner slope of the projected mass-density profile ($S_{50\text{–}200}$), color coded by M_{500}. Clusters without an M_{500} estimate are plotted in white. *Middle right:* Cluster redshift, color coded by $S_{50\text{–}200}$. *Bottom left:* Effective Einstein area ($\pi\theta_{\rm E}^2$), color coded by M_{500}. Clusters without an M_{500} estimate are plotted in white. The curves show the expected relationship for different potentials at a redshift of $z_{\rm lens} = 0.5$ and no ellipticity. Maroon shows an SIS distribution; blue shows a PIEMD, with a core radius of 40 kpc, and a cut radius of 1500 kpc; purple shows an NFW profile with a scale radius of 100 kpc. *Bottom right:* Distance between the BCG and farthest bright arc ($\theta_{\rm arc}$). The shape of the data points indicates different lens-modeling algorithms, where light gray lines connect models of the same cluster modeled by different algorithms. The three GLAFIC models where 5% was added to the upper error bar due to the limited field of view are given a dashed black border. In all panels, red error bars indicate models without spectroscopic redshift constraints or if it is not known whether a spectroscopic constraint is used.

PIEMD and NFW models, the relationship is similar, but also dependent on the characteristic radii chosen. For these two cases, the radius at which the slope of the curve flattens increases with an increasing core or scale radius. For many of the clusters in our sample, the mass distribution is much more complicated than a singular halo with no ellipticity, greatly influencing the extent of significantly magnified area. Although $\mathcal{A}_{|\mu|\geqslant 3}$ and $\pi\theta_{\rm E}^2$ are clearly interconnected, we choose to focus on $\mathcal{A}_{|\mu|\geqslant 3}$ because it captures a diversity of lens properties' effect on the magnified area that the commonly used Einstein radius may miss.

3.6. Distance to Farthest Bright Arc

The observed radial extent of lensing evidence is often used as a proxy of the Einstein radius, and thus the lensing power of a cluster. We test the efficacy of this indicator by comparing the separation between the BCG and the farthest bright arc, which we denote as $\theta_{\rm arc}$, to the lensing strength. By construction, the SGAS clusters are a prime sample for testing this assessment, as they were identified based on the observation of a giant bright arc in their field. We use the HST images to find and measure $\theta_{\rm arc}$ for each SGAS cluster. We measure $\theta_{\rm arc}$ in 17 RELICS and HFF clusters, in which a bright arc can be easily identified; if more than one bright arc is observed, we select the one farthest from the chosen BCG. Because only a fraction of the sample is included in this test, we do not include $\theta_{\rm arc}$ in Table 1 or Figure 2.

3.7. Statistical Indicators

We use the Kendall τ and Spearman r rank correlation coefficients to assess the existence of correlations between parameters that were evaluated in this work. There are several RELICS and HFF clusters for which we use results from multiple modeling algorithms. When computing Kendall τ and Spearman r coefficients, we avoid double-counting these clusters by computing the coefficients 10,000 times, each time randomly drawing the model used for each cluster with more than one model. We report the mean value of the computed coefficients across the 10,000 trials and the mean p-value. There are a few other ways to consider these clusters with multiple models. We tested three methods: (1) Using all models, each having equal weight. (2) Using one model per cluster, e.g., prioritizing `Lenstool` and using other algorithms if the highest-priority one is unavailable. (3) Including all models for each cluster, but giving less weight to multiple models of the same cluster, so that each cluster as a whole has equal weight. We find that the computed Kendall τ and Spearman r coefficients are very similar across these methods and therefore the conclusions are not affected by these choices.

4. Results and Discussion

In this section we investigate the dependence of our normalized lensing-strength indicator ($\mathcal{A}^{0.5}_{|\mu|\geqslant 3}$) on the large-scale mass (M_{500}), the strong-lensing core mass ($M_{\rm SL}$(200kpc)), the inner slope of the projected mass-density profile ($S_{50\text{–}200}$), the effective Einstein area ($\pi\theta_{\rm E}^2$), and the separation between the BCG and farthest bright arc ($\theta_{\rm arc}$). We discuss our results and compare our findings with previous studies.

4.1. Large-scale Mass (M_{500})

In the top left panel of Figure 4 we plot the normalized lensing strength against M_{500}, a large-scale mass estimate that is measured independently of the lensing analyses. Light gray vertical lines connect models of the same cluster that were obtained with different techniques. We find clusters with low lensing strength across the entire mass range. Furthermore, clusters with a given mass span a broad range of lensing strengths, particularly for $M_{500} \approx 11 \times 10^{14}$ $M_\odot$, implying that a high mass does not guarantee a high lensing strength. We compute Kendall τ and Spearman r coefficients of 0.26 and 0.36, respectively , with p-values < 0.01.

Salmon et al. (2020) reported the high-z candidates found by the RELICS project. They found little to no correlation between M_{500} and the number of $z \sim 6-8$ candidates discovered. High-mass clusters, such as the massive lens MACS J0417.5 1154, often produced hardly any $z \sim 6-8$ candidates. Our result is consistent with this observation, i.e., a high total mass is not necessarily an indicator of a high lensing strength. This result is also in agreement with Cerny et al. (2018) who computed lens models for five clusters in the RELICS survey and found that the magnified source-plane area (proxy for lensing efficiency), is not a simple function of the total mass of a cluster. For instance, Abell 2163 provides a relatively low magnification area, despite having the highest Planck SZ mass of the sample.

4.2. Strong-lensing Core Mass (M_{SL}(200kpc))

We observe a high probability of correlation ($\tau = 0.66$ and $r = 0.84$, with p-values < 0.01) between the inner-core mass and normalized lensing strength, shown in the top right panel of Figure 4. As noted in Section 3.3, this is expected, as the inner-core mass is directly responsible for the strong-lensing effect; however, we note a large spread in lensing strengths. Furthermore, we note that the lower bound of the observed lensing strength increases with inner-core mass, as can be inferred from the absence of clusters in the bottom right region of the plot.

4.3. Inner Slope of Projected Mass-density Profile ($S_{50\text{–}200}$)

We show in the middle left panel of Figure 4 the normalized lensing strength against the slope of the projected mass-density profile ($S_{50\text{–}200}$). Light gray lines connect models of the same cluster produced with different algorithms. Flat profiles (high $S_{50\text{–}200}$) show the largest range of lensing strengths, including the highest values. We note that the upper left corner of the diagram, indicating the steep slope and high lensing-strength region, is not populated. At steeper slopes (low $S_{50\text{–}200}$), the highest lensing strength measured diminishes. This suggests that the slope of the projected mass-density profile can be an indicator of the maximum possible lensing strength of a cluster, with the highest lensing strengths only found in clusters with flatter inner profiles. We compute Kendall τ and Spearman r coefficients of 0.53 and 0.71, respectively, with p-values < 0.01. Notably, the measured correlation coefficients are greater than those for the large-scale mass, suggesting a higher probability of correlation.

We note that the slope measured in models of the same cluster computed with different techniques often differ (e.g., PLCK G171.9-40.7, PLCK G287.0+32.9); however, the differences tend to follow the trend of a flatter slope having a higher lensing strength.

The importance of the shape of the projected mass-density profile can help explain why there is no significant correlation between M_{500} and lensing strength. Strong lensing requires surpassing a critical threshold of high surface density. Flatter profiles that already reach the critical threshold could therefore offer a larger magnification area than steeper profiles because the density drops off slower with radius, boosting their lensing strengths. Comparing two strong-lensing clusters with the same total mass, the cluster with a flatter profile would enable a larger lensing-strength region, as more area is above the critical density, despite the peak density being less than that of the cluster with a steeper profile. Cluster physical properties such as substructure, ellipticity, and merging events could flatten the profile, enabling a more elongated area of critical density. Furthermore, if two strong-lensing clusters have the same inner slope, the cluster with the higher mass could provide a larger lensing-strength area by enabling more area to be of critical density.

We see little to no stratification by large-scale mass in the normalized lensing strength versus inner slope plot (middle left panel of Figure 4). This further suggests that several physical properties affect the lensing strength of a cluster. $S_{50\text{–}200}$ is an attempt to capture several properties by characterizing the shape of the projected mass-density profile at the core of the galaxy cluster. The overall trend we find hints to an interesting combination of physical cluster properties leading to the overall lensing strength of the cluster. Future studies can explore more rigorous assessments of the mass-density profile and other physical cluster properties to further investigate what dominates lensing strength. Additionally, we note that we find a low probability of correlation between the inner slope and large-scale mass (Kendall $\tau = 0.17$, Spearman $r = 0.23$, with p-values < 0.1), as seen in Figure 5. M_{500} and $S_{50\text{–}200}$ represent very different cluster-centric regimes, suggesting properties of different scales do not need to be well correlated. We find that a high large-scale mass does not imply a flat inner slope or a high lensing strength.

The age of the structure may also play a role in the relation between lensing strength and the inner slope we measure. As a cluster ages, we expect the mass-density profile to become more cuspy as the cluster relaxes, becoming more centralized and drawing more mass into the center of the potential well. We therefore expect a cluster to move diagonally toward the

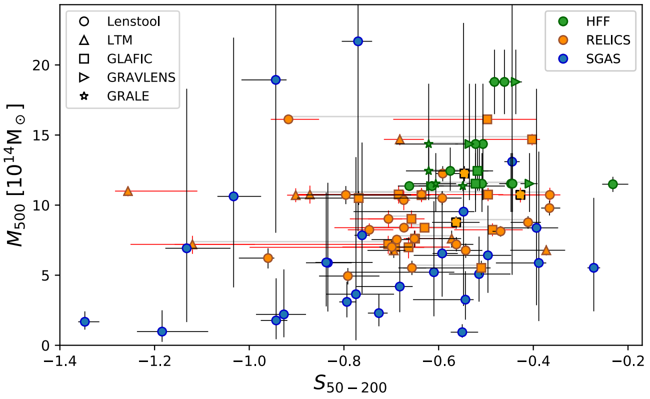

Figure 5. Large-scale mass estimate (M_{500}), which is measured independently of the lensing analyses, compared with the inner slope of the projected mass-density profile, measured in between 50 and 200 kpc from the BCG. Color coding and shape refer to different samples of clusters and different lens-modeling algorithms, respectively. Light gray horizontal lines connect models of the same cluster, computed with different algorithms. Red error bars indicate models without spectroscopic redshift constraints or if it is not known whether a spectroscopic constraint is used. No obvious correlation is found between the two indicators.

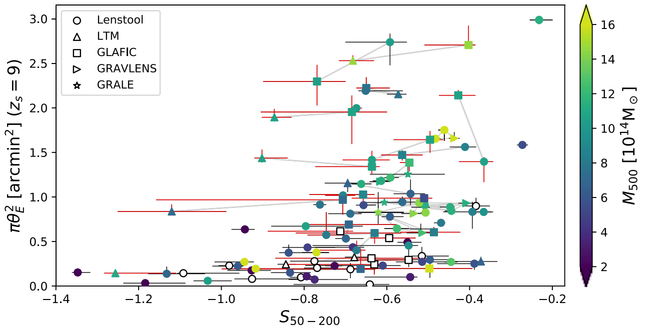

Figure 6. Effective Einstein area for a source at $z_s = 9$ compared with the inner slope of the projected mass-density profile, measured in between 50 and 200 kpc from the BCG. Color coding shows the large-scale mass estimate (M_{500}), which is measured independently of the lensing analyses. Clusters without an M_{500} estimate are plotted in white. Shape refers to different lens-modeling algorithms and light gray lines connect models of the same cluster modeled by different algorithms. Red error bars indicate models without spectroscopic redshift constraints or if it is not known whether a spectroscopic constraint is used. This plot shows how effective Einstein area relates less strongly to the slope because it does not capture high magnification regions far from the critical curve.

bottom left of the normalized lensing strength versus inner slope plot (middle left panel of Figure 4) over cosmic time as the slope steepens and lensing strength lessens. In a more disturbed cluster, such as a major merger with a flat profile, over time the magnification area will radically evolve due to the evolution of the 2D projection of the mass distribution (Redlich et al. 2012). The cluster may greatly increase in lensing strength through the merging process, but decrease as the profile steepens in the more centralized merged cluster.

Although we correct for the redshift dependence on how the lensing-strength area projects onto our sky, cluster redshift can still play a role in lensing strength. We note that the normalized lensing strength—slope relation we observe persists across the range of cluster redshifts, as shown in the middle right panel of Figure 4, which compares the normalized lensing strength with cluster redshift, color coded by $S_{50–200}$.

The finding that a high lensing strength is possible only in clusters with flatter inner profiles does not conflict with the consensus that lensing clusters tend to be more concentrated. The samples of clusters that are investigated here are lensing-selected, and as such are likely to already be highly concentrated. The concentration is defined as $c = r_\triangle / r_s$, where $r_\triangle$ is the radius of interest and r_s is the scale radius. Higher-concentration means that a higher fraction of the total mass is contained in the cluster core. The inner slope, $S_{50–200}$, is measured at much smaller projected radii, and represents the slope of the projected mass density inner to the r_s range. For reference, r_{500} in our sample ranges from 556 kpc to 1676 kpc. Oguri & Blandford (2009) illustrate these characteristic scales compared with the Einstein radius (see their Figure 1).

4.4. Effective Einstein Radius ($e\theta_E$) and Area ($\pi\theta_E^2$)

We plot the normalized lensing strength against the effective Einstein area for $z_s = 9$ in the bottom left panel of Figure 4, color coded by M_{500}. Although we use the normalized lensing strength here, in the Appendix we show the corresponding plot with both measurements shown in their native cluster redshift, i.e., not normalized for the redshift dependence of area projection onto the sky. We note that the conclusions are independent of this choice.

We observe a relation between the normalized lensing strength and effective Einstein area, with a scatter indicative of how much the region of $|\mu| \geqslant 3$ extends from the main tangential critical curve, which depends on the physical properties of a cluster that affect the gradient of the magnification. We compute Kendall τ and Spearman r coefficients of 0.68 and 0.86, respectively, with p-values < 0.01, suggesting a strong probability of correlation. The normalized lensing strength and effective Einstein area generally increase with mass, but a high mass does not guarantee a high lensing strength.

Due to the correlation between the effective Einstein area and the normalized lensing strength, they show similar trends with large-scale mass, inner-core mass, and the slope of the projected mass-density profile. In Figure 6 we compare the effective Einstein area for $z_s = 9$ with $S_{50–200}$, color coded by the large-scale mass estimate (M_{500}), which was measured independently of the lensing analysis.

We find that $e\theta_E$ has a lower probability of correlation with the inner slope than our lensing-strength indicator does. This suggests that the slope has a stronger impact on regions farther from the very inner core, a flat profile enabling more area far from the tangential critical curve to be moderately magnified. Our lensing-strength indicators, $\mathcal{A}^{\mathrm{lens}}_{|\mu|\geqslant 3}$ and $\mathcal{A}^{0.5}_{|\mu|\geqslant 3}$, better capture the magnification potential of a cluster, accounting for the lower magnification regions that extend farther from the critical curve, and provide an important boost in high-z survey volume.

4.5. Distance to Farthest Bright Arc (θ_{arc})

In the bottom right panel of Figure 4 we plot the normalized lensing strength against the distance between the BCG and the farthest identified bright arc (θ_{arc}). As in Section 4.4, we use the normalized lensing strength here, but show in the Appendix the corresponding plot with both measurements in their native cluster redshift, i.e., not normalized for the redshift dependence of area projection onto the sky. The conclusions are again independent of this choice.

We find that clusters with low $\theta_{\rm arc}$ span a broad range of lensing strengths, and could not define powerful lenses. However, all clusters with $\theta_{\rm arc} \gtrsim 30\farcs0$ have moderate to high lensing strengths, implying that an observation of large $\theta_{\rm arc}$ may be used as a direct observational indicator to identify and select powerful lenses. Overall, we compute Kendall τ and Spearman r coefficients of 0.39 and 0.55, respectively, with p-values < 0.01.

5. Summary and Conclusions

We present an analysis of lensing strength across a sample of 110 strong-lensing models of 74 cluster fields from the HFF, RELICS, and SGAS programs. We use as an indicator of lensing strength the area on the sky with moderate to high magnification that a cluster provides, which facilitates the search for magnified high-redshift galaxies. The lensing strength, $\mathcal{A}^{0.5}_{|\mu|\geqslant 3}$, is defined as the image-plane area with absolute magnification of at least three for a source at $z_s = 9$, corrected for the cluster redshift to account for the redshift dependence of area projection onto the sky. We compare the normalized lensing strength to the large-scale mass, inner-core projected mass, inner slope of the projected mass-density profile, effective Einstein area, and distance between the BCG and the farthest bright arc detected in the field. The results of this analysis are summarized as follows:

1. We find that a high large-scale mass (M_{500}) does not guarantee a high lensing strength ($\mathcal{A}^{0.5}_{|\mu|\geqslant 3}$) . We observe more clusters with a high lensing strength as large-scale mass increases, but find low lensing-strength clusters across the entire mass range, including high-mass lensing clusters with a low lensing strength.
2. As expected, the lensing strength has a high probability of correlation with the projected aperture mass within 200 kpc of the BCG, computed from the strong-lensing model.
3. We find that the lensing-strength indicator, $\mathcal{A}^{0.5}_{|\mu|\geqslant 3}$, has a high probability of correlation with the inner slope of the projected mass-density profile, measured in an annulus between 50 and 200 kpc from the BCG (S_{50-200}). Notably, the probability of correlation with lensing strength is higher than for large-scale mass (M_{500}). Flatter profiles offer a wide range of lensing strengths, whereas the maximum lensing strength observed diminishes for steeper profiles (middle left panel of Figure 4). No cluster is found to have a steep profile and a high lensing strength, leaving the top left region of the lensing strength versus inner slope plot empty.
4. The lensing-strength indicator, $\mathcal{A}^{0.5}_{|\mu|\geqslant 3}$, has a high probability of correlation with effective Einstein area ($\pi\theta_{\rm E}^2$). The scatter between these indicators stems from the intrinsic variance of cluster properties that determine the extent of significant magnification beyond the tangential critical curve. The lensing-strength indicator captures the significantly magnified regions that extend farther from the tangential critical curve.
5. We find clusters with a short distance between the BCG and farthest bright arc ($30\farcs0 \gtrsim \theta_{\rm arc}$) to have a wide range of lensing strength; however, all clusters with $\theta_{\rm arc} \gtrsim 30\farcs0$ are powerful lenses with a high lensing strength.

Studies of the dependence of lensing strength on physical cluster properties can aid the selection of lensing clusters for future surveys, including criteria beyond mass proxies. Maximizing lensing strength provides a greater opportunity to find high-redshift candidates that give insight into the early universe. Furthermore, the absence of clusters with a steep profile and high lensing strength could help constrain cosmology. Our results would support cosmologies that do not produce clusters with steep inner profiles and high lensing strengths at the current age of the universe. A future study could assess how the lensing strength–inner slope relation appears in simulations for different cosmologies and how the relation changes as the universe ages.

This paper demonstrates, from a sample of 74 clusters with strong lens models, that the efficacy of galaxy clusters as efficient cosmic telescopes cannot be solely determined from global properties like their total mass or redshift. Lensing-assisted high-z surveys that select lenses by mass alone will not be optimized for lensing strength, as some fraction of the high-mass clusters may have low lensing strengths: high lensing efficiency requires strong-lensing clusters whose projected mass distribution has a shallow inner slope.

We thank Dan Coe for useful discussion and helpful comments. We thank the HFF, RELICS, and SGAS projects for making their lens models publicly available. Some of the High Level Science Products (HLSP) presented in this paper were obtained from the Mikulski Archive for Space Telescopes (MAST). STScI is operated by the Association of Universities for Research in Astronomy, Inc., under NASA contract NAS5-26555. J.D.R.G. acknowledges support by the National Science Foundation Graduate Research Fellowship Program under grant No. DGE 1256260. G.M. received funding from the European Unions Horizon 2020 research and innovation program under the Marie Skodowska-Curie grant agreement No MARACAS—DLV-896778.

Appendix A
Gallery of Clusters

In Figure 7 we provide a gallery of color images for each cluster. Green circles mark 50 kpc and 200 kpc from the BCG assumed. We include the slope and normalized lensing strength. White contours mark the projected mass density at $\kappa = 1$, scaled to $D_{LS}/D_S = 1$. Cyan contours mark the magnification at $|\mu| \geqslant 3$. The effective Einstein radius is shown in magenta. `Lenstool` models are used where available (using the Sharon models for the HFF clusters), LTM if there is no `Lenstool` model, and GLAFIC if there is no `Lenstool` or LTM model. Clusters are ordered by slope, from flattest to steepest.

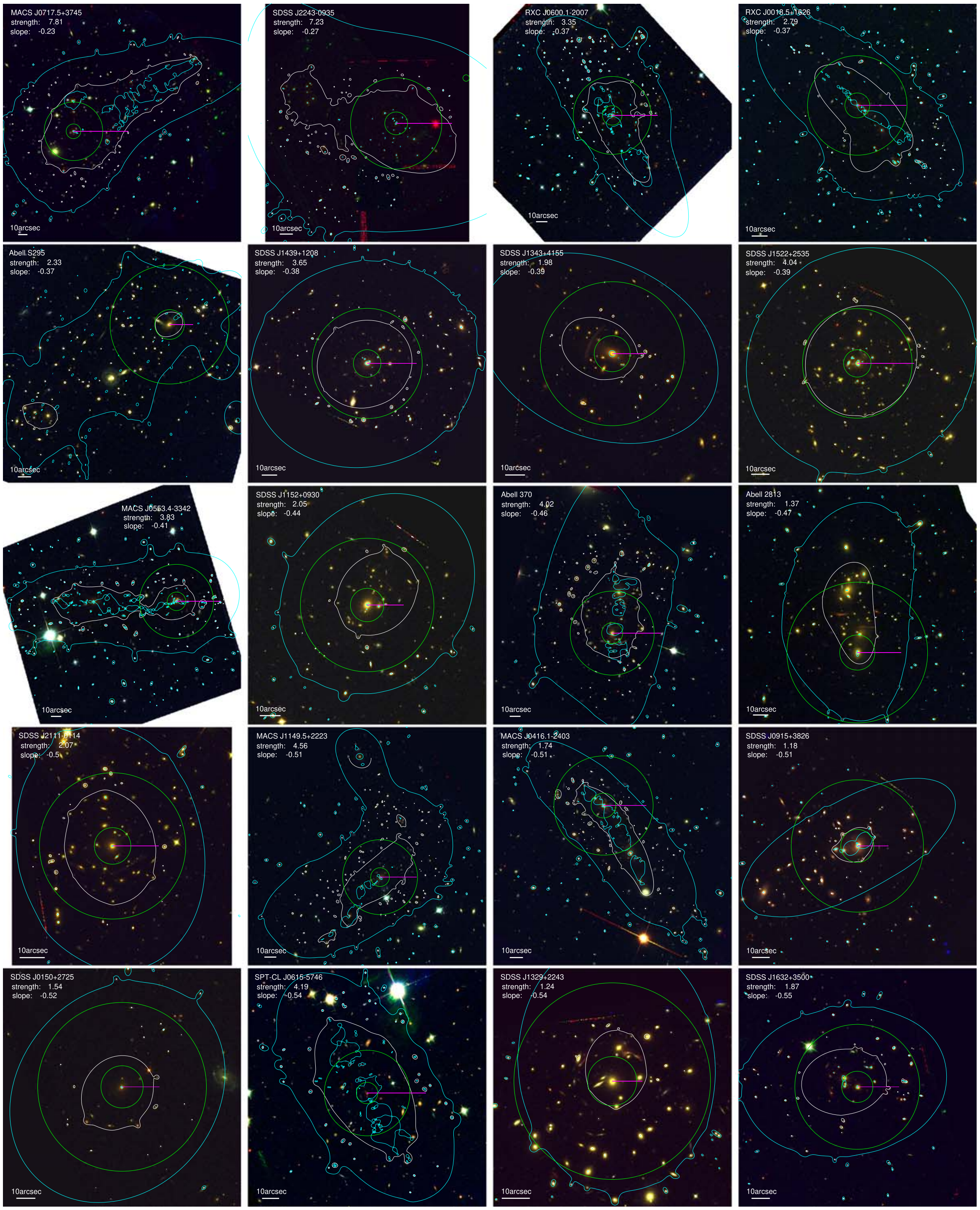

Figure 7. Composite color images of the clusters MACS J0717.5+3745, SDSS J2243 0935, RXC J0600.1−2007, RXC J0018.5+1626, Abell S295, SDSS J1439+1208, SDSS J1343+4155, SDSS J1522+2535, MACS J0553.4−3342, SDSS J1152+0930, Abell 370, Abell 2813, SDSS J2111 0114, MACS J1149.5+2223, MACS J0416.1−2403, SDSS J0915+3826, SDSS J0150+2725, SPT−CL J0615−5746, SDSS J1329+2243, SDSS J1632+3500, SDSS J1050+0017, Abell 3192, Abell 2744, Abell 1758aNW, MACS J0417.5−1154, RXC J2211.7−0350, SDSS J1420+3955, Abell S1063, Abell 1758aSE, RXS J060313.4+4212−N, ACT−CLJ0102−49151, SDSS J0108+0624, RXC J0032.1+1808, RXC J0911.1+1746, Abell 2537, SMACS J0723.3−7327, RXC J0232.2−4420, PLCK G287.0+32.9, SDSS J0851+3331, RXS J060313.4+4212−S, SDSS J1156+1911, PLCK G004.5−19.5, MACS J0035.4−2015, RXC J0142.9+4438, SDSS J1621+0607, SDSS J1110+6459, RXC J0949.8+1707, SDSS J1209+2640, CL J0152.7−1357, SDSS J1336 0331, MS 1008.1−1224, SDSS J1152+3313, PLCK G209.79+10.23, SDSS J1115+1645, SDSS J1531+3414, SDSS J0928+2031, MACS J0025.4−1222, MACS J0308.9+2645, PLCK G171.9+40.7, Abell 2163, SDSS J1723+3411, SDSS J0952+3434, SDSS J1055+5547, SDSS J1456+5702, MACS J0257.1−2325, SDSS J0146 0929, SDSS J0957+0509, SDSS J0333 0651, MACS J0159.8−0849, SDSS J1604+2244, SDSS J0004 0103, Abell 697, and SDSS J1038+4849. Green circles show radii of 50 kpc and 200 kpc from the BCG, the range for the inner-slope measurement. For each cluster, the normalized lensing strength ($\mathcal{A}^{0.5}_{|\mu|\geqslant 3}$) and inner slope ($S_{50-200}$) are listed. White contours mark the mass density at $\kappa = 1$, where κ is scaled to $D_{LS}/D_S = 1$. Cyan contours mark the magnification at $|\mu| \geqslant 3$. The effective Einstein radius is shown in magenta. `Lenstool` models are used where available (using the Sharon models for the HFF clusters), LTM if there is no `Lenstool` model, and GLAFIC if no `Lenstool` or LTM model is available. Clusters are ordered left to right and top to bottom by slope, from flattest to steepest. North is up and east is left in all panels. A 10$''\!.$0 scale is found in each panel for size reference.

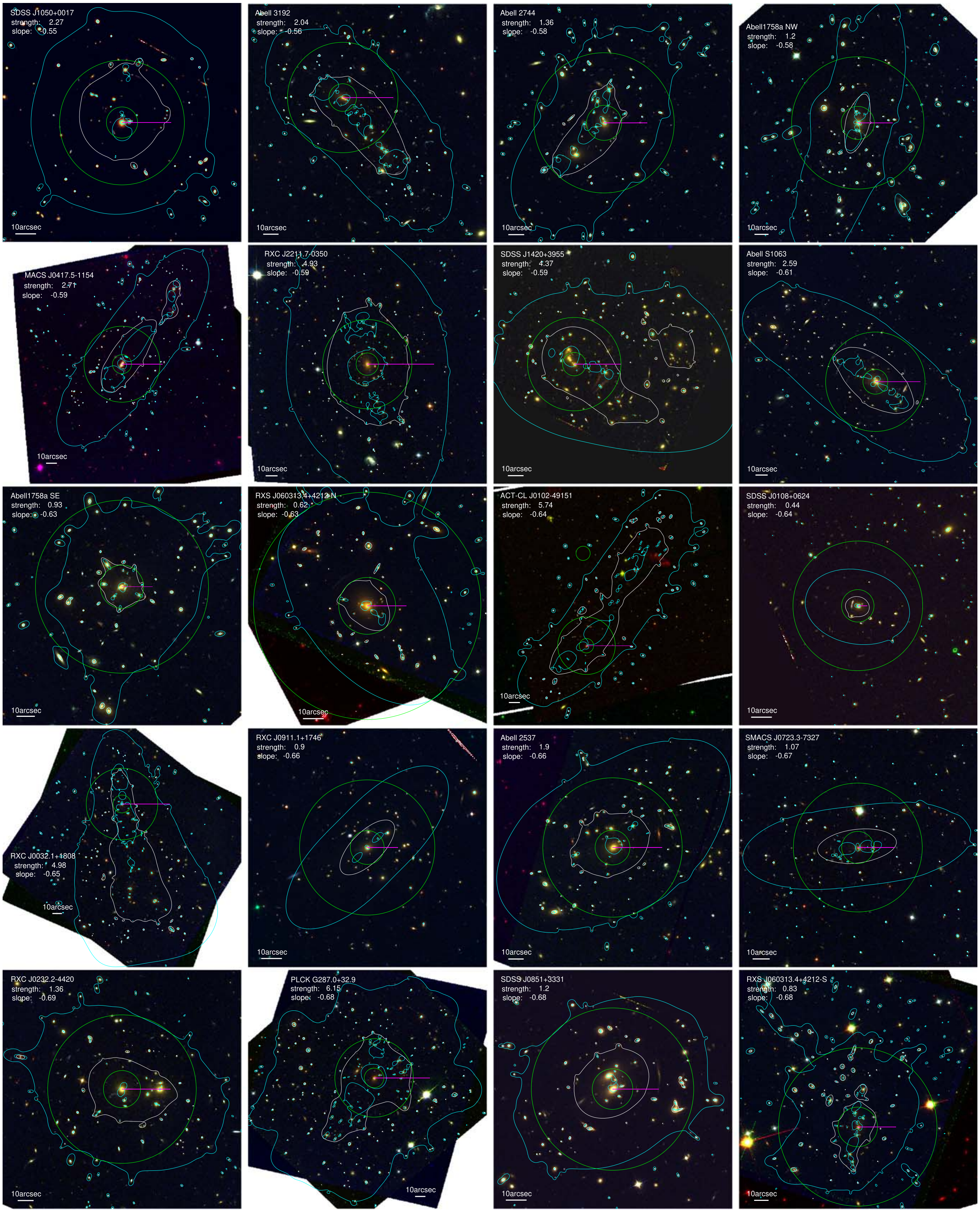

Figure 7. (Continued.)

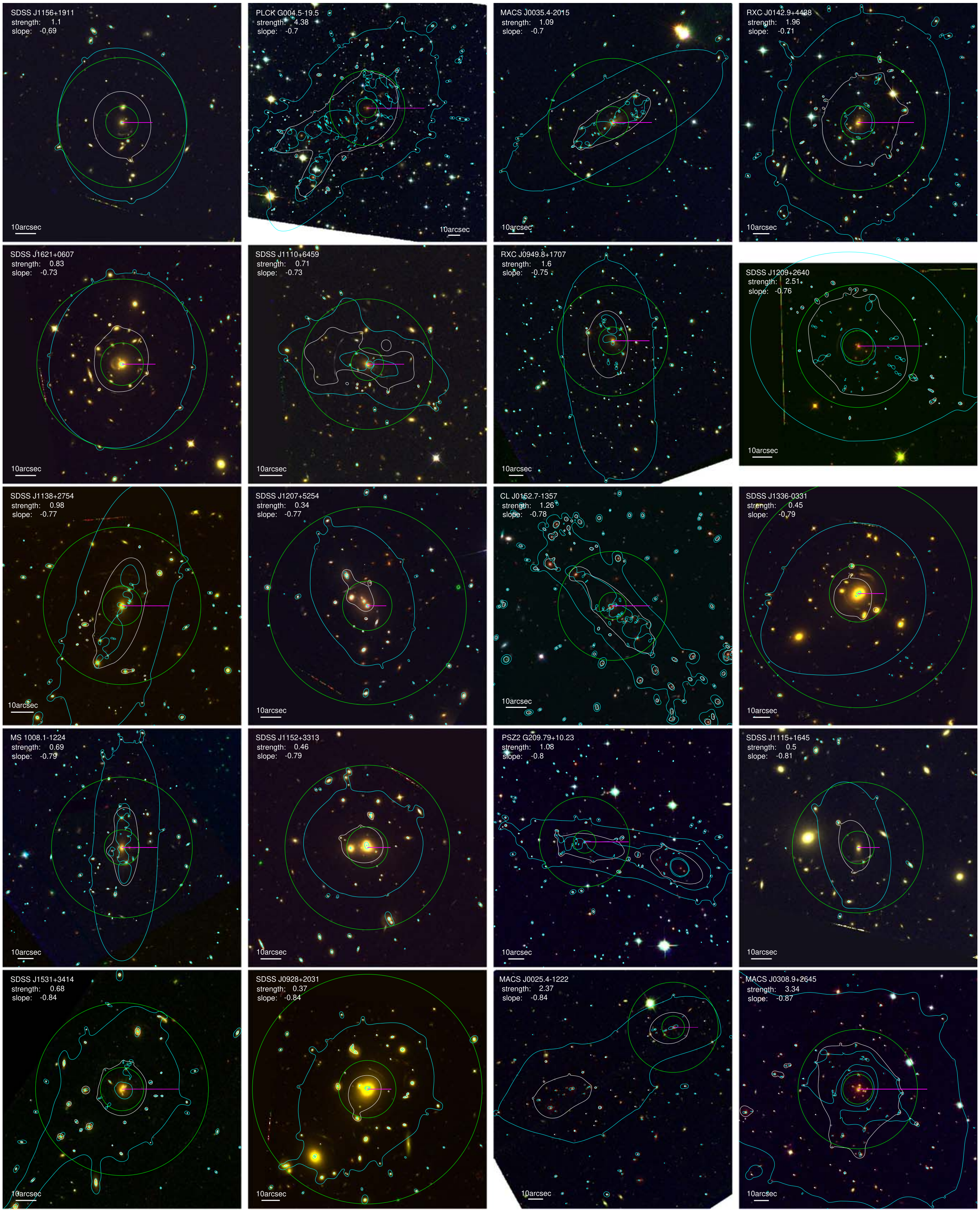

Figure 7. (Continued.)

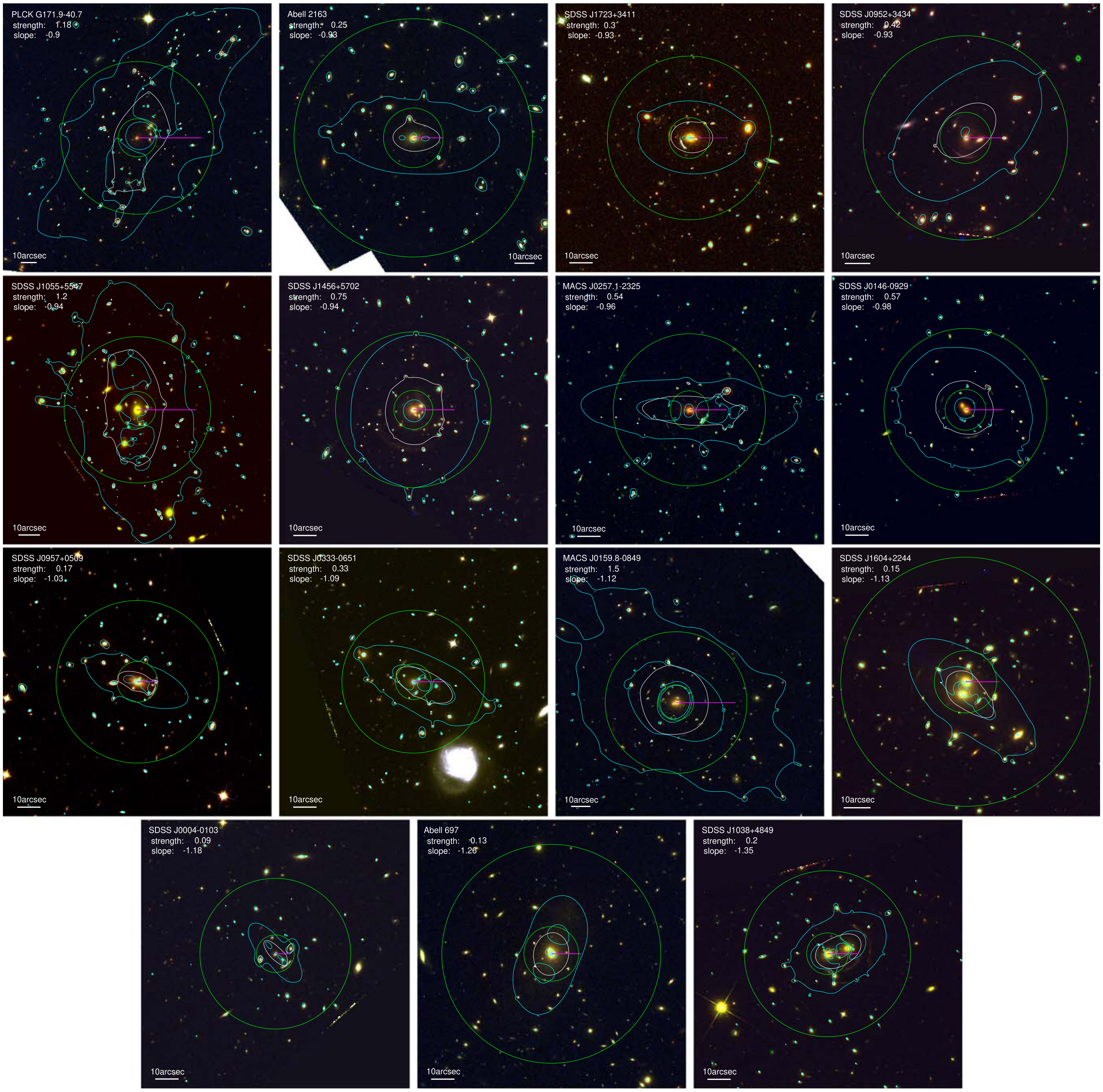

Figure 7. (Continued.)

Appendix B
Comparisons with Nonnormalized Lensing Strength

In order to compare cluster properties to lensing strength, we corrected for the redshift dependence of area projection onto the sky, converting all lensing strengths ($\mathcal{A}^{\text{lens}}_{|\mu|\geqslant 3}$) to their corresponding values if the lensing-strength area was projected onto the sky from a redshift of 0.5 ($\mathcal{A}^{0.5}_{|\mu|\geqslant 3}$). In Figure 8 we provide comparisons to lensing strength with the nonnormalized value.

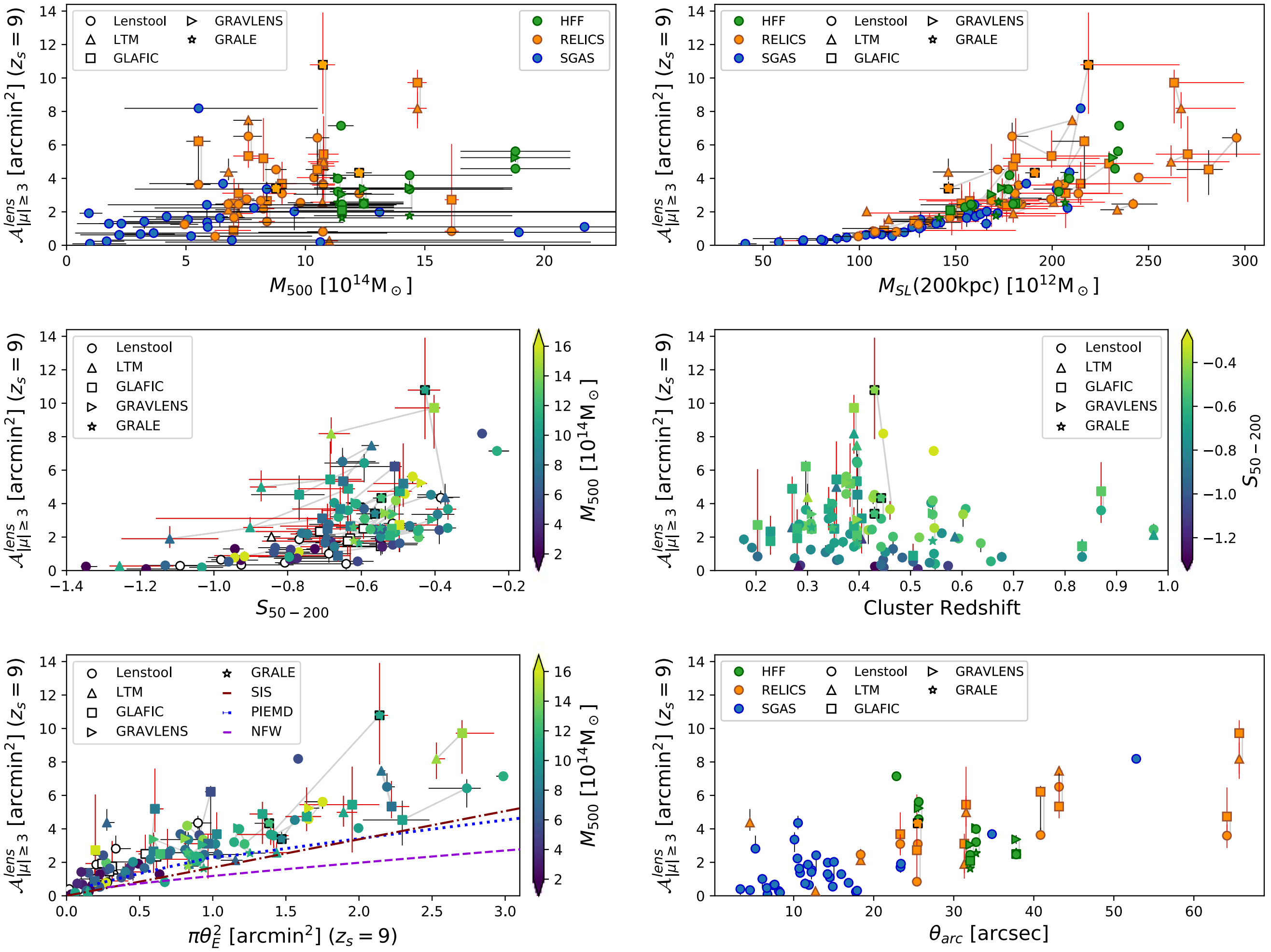

Figure 8. Nonnormalized lensing strength ($\mathcal{A}^{\text{lens}}_{|\mu|\geqslant 3}$) compared with cluster properties. *Top left:* Large-scale mass estimate (M_{500}), which is measured independently of the lensing analyses. *Top right:* Projected mass within 200 kpc of the BCG (M_{SL}(200kpc)). *Middle left:* Inner slope of the projected mass-density profile ($S_{50\text{–}200}$), color coded by M_{500}. Clusters without an M_{500} estimate are plotted in white. *Middle right:* Cluster redshift, color coded by $S_{50\text{–}200}$. *Bottom left:* Effective Einstein area ($\pi\theta^2_{\text{E}}$), color coded by M_{500}. Clusters without an M_{500} estimate are plotted in white. The curves show the expected relationship for different potentials at a redshift of $z_{\text{lens}} = 0.5$, and no ellipticity. Maroon shows an SIS distribution; blue shows a PIEMD with a core radius of 40 kpc, and a cut radius of 1500 kpc; purple shows an NFW profile with a scale radius of 100 kpc. *Bottom right:* Distance between the BCG and farthest bright arc (θ_{arc}). The shape of the data points indicates different lens-modeling algorithms and light gray lines connect models of the same cluster modeled by different algorithms. The three GLAFIC models where 5% was added to the upper error bar due to the limited field of view are given a dashed black border. In all panels, red error bars indicate models without spectroscopic constraints or if it is not known whether a spectroscopic constraint is used.

Appendix C
Comparisons with M_{200}

Throughout this paper we focus our analysis on M_{500}. In Figure 9, we provide plots for comparison with M_{200} for reference. To obtain an M_{200} estimate for clusters included in the RELICS program, we solve for the M_{200} value corresponding to the Planck SZ M_{500} mass by means of the process outlined in Section 3.2. The same is done for Abell S1063 and MACS J0717.5+3745. For MACS J1149.5+2223, MACS J0416.1−2403, and Abell 2744, we use the M_{500} computed from the X-ray temperature to solve for the corresponding M_{200}. For Abell 370, we use the M_{200} estimate reported in Umetsu et al. (2011). The median M_{200} value is used for the SGAS clusters.

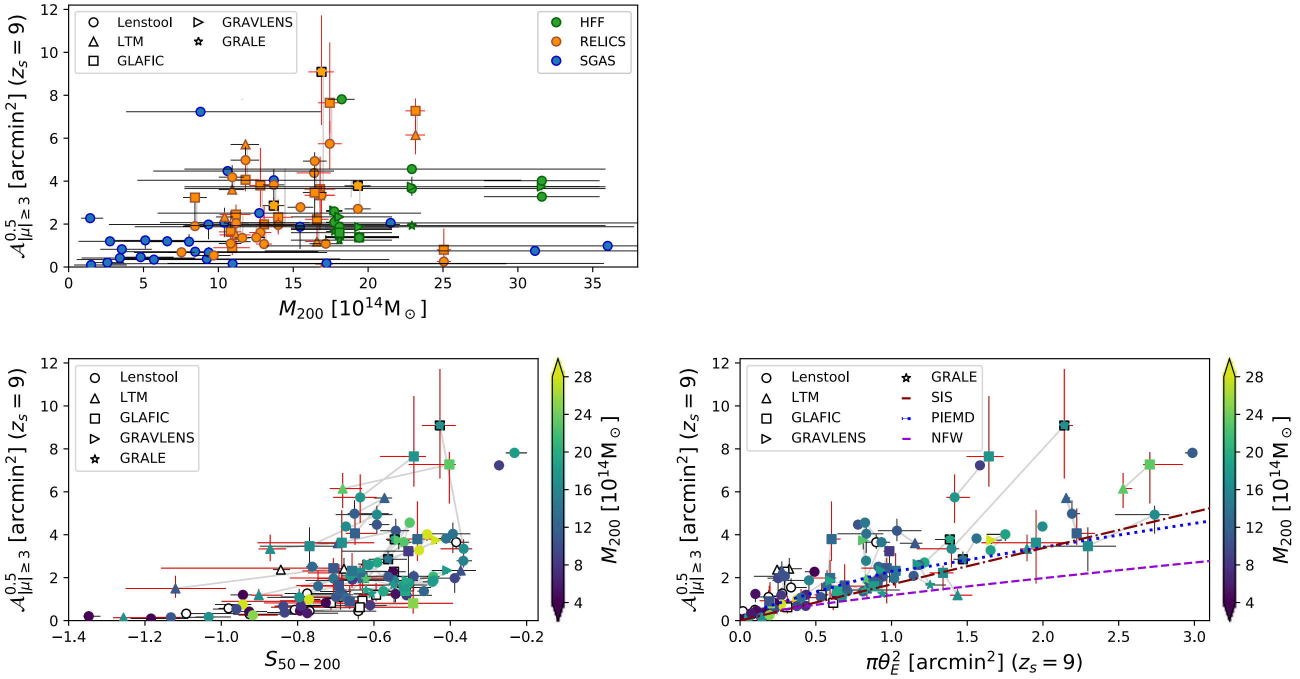

Figure 9. Normalized lensing strength ($\mathcal{A}^{0.5}_{|\mu|\geqslant 3}$) compared with cluster properties, with M_{200} as the large-scale mass estimate. *Top left:* Large-scale mass estimate (M_{200}), which is measured independently of the lensing analyses. *Bottom left:* Inner slope of the projected mass-density profile ($S_{50–200}$), color coded by M_{200}. Clusters without an M_{200} estimate are plotted in white. *Bottom right:* Effective Einstein area ($\pi\theta_{\rm E}^2$), color coded by M_{200}. Clusters without an M_{200} estimate are plotted in white. The curves show the expected relationship for different potentials at a redshift of $z_{\rm lens} = 0.5$, and no ellipticity. Maroon shows an SIS distribution; plue shows a PIEMD with a core radius of 40 kpc, and a cut radius of 1500 kpc; purple shows an NFW profile with a scale radius of 100 kpc. The shape of the data points indicates different lens-modeling algorithms and light gray lines connect models of the same cluster modeled by different algorithms. The three GLAFIC models where 5% was added to the upper error bar due to the limited field of view are given a dashed black border. In all panels, red error bars indicate models without spectroscopic constraints or if it is not known whether a spectroscopic constraint is used.

ORCID iDs

Carter Fox https://orcid.org/0000-0001-8316-9482
Guillaume Mahler https://orcid.org/0000-0003-3266-2001
Keren Sharon https://orcid.org/0000-0002-7559-0864
Juan D. Remolina González https://orcid.org/0000-0002-7868-9827

References

Acebron, A., Cibirka, N., Zitrin, A., et al. 2018, ApJ, 858, 42
Acebron, A., Alon, M., Zitrin, A., et al. 2019, ApJ, 874, 132
Acebron, A., Zitrin, A., Coe, D., et al. 2020, ApJ, 898, 6
Albert, J. G., Sifón, C., Stroe, A., et al. 2017, A&A, 607, A4
Allen, S. W. 1998, MNRAS, 296, 392
Arnaud, M., Pointecouteau, E., & Pratt, G. W. 2007, A&A, 474, L37
Bartelmann, M., & Meneghetti, M. 2004, A&A, 418, 413
Bartelmann, M., Meneghetti, M., Perrotta, F., Baccigalupi, C., & Moscardini, L. 2003, A&A, 409, 449
Bartelmann, M., & Weiss, A. 1994, A&A, 287, 1
Bayliss, M. B., Hennawi, J. F., Gladders, M. D., et al. 2011, ApJS, 193, 8
Bayliss, M. B., Johnson, T., Gladders, M. D., Sharon, K., & Oguri, M. 2014, ApJ, 783, 41
Bayliss, M. B., Sharon, K., & Johnson, T. 2015, ApJL, 802, L9
Beers, T. C., Flynn, K., & Gebhardt, K. 1990, AJ, 100, 32
Blanchard, P. K., Bayliss, M. B., McDonald, M., et al. 2013, ApJ, 772, 24
Blanton, M. R., Bershady, M. A., Abolfathi, B., et al. 2017, AJ, 154, 28
Boldrin, M., Giocoli, C., Meneghetti, M., et al. 2016, MNRAS, 457, 2738
Bonamigo, M., Grillo, C., Ettori, S., et al. 2018, ApJ, 864, 98
Caminha, G. B., Grillo, C., Rosati, P., et al. 2016, A&A, 587, A80
Caminha, G. B., Grillo, C., Rosati, P., et al. 2017, A&A, 600, A90
Caminha, G. B., Rosati, P., Grillo, C., et al. 2019, A&A, 632, A36
Cerny, C., Sharon, K., Andrade-Santos, F., et al. 2018, ApJ, 859, 159
Child, H. L., Habib, S., Heitmann, K., et al. 2018, ApJ, 859, 55
Cibirka, N., Acebron, A., Zitrin, A., et al. 2018, ApJ, 863, 145
Coe, D., Salmon, B., Bradač, M., et al. 2019, ApJ, 884, 85
Cypriano, E. S., Sodré, Laerte, J., Campusano, L. E., et al. 2001, AJ, 121, 10
Dalal, N., Holder, G., & Hennawi, J. F. 2004, ApJ, 609, 50
Dalal, N., & Keeton, C. R. 2003, arXiv:astro-ph/0312072
D'Aloisio, A., & Natarajan, P. 2011, MNRAS, 415, 1913
Diehl, H. T., Buckley-Geer, E. J., Lindgren, K. A., et al. 2017, ApJS, 232, 15
Ebeling, H., Edge, A. C., & Henry, J. P. 2001, ApJ, 553, 668
Evrard, A. E., Bialek, J., Busha, M., et al. 2008, ApJ, 672, 122
Fedeli, C., Bartelmann, M., Meneghetti, M., & Moscardini, L. 2007, A&A, 473, 715
Fedeli, C., Bartelmann, M., Meneghetti, M., & Moscardini, L. 2008, A&A, 486, 35
Futamase, T., Hattori, M., & Hamana, T. 1998, ApJL, 508, L47
Giocoli, C., Meneghetti, M., Bartelmann, M., Moscardini, L., & Boldrin, M. 2012, MNRAS, 421, 3343
Gladders, M. D., Hoekstra, H., Yee, H. K. C., Hall, P. B., & Barrientos, L. F. 2003, ApJ, 593, 48
Gladders, M. D., & Yee, H. K. C. 2005, ApJS, 157, 1
Gralla, M. B., Sharon, K., Gladders, M. D., et al. 2011, ApJ, 737, 74
Grillo, C., Suyu, S. H., Rosati, P., et al. 2015, ApJ, 800, 38
Harvey, D., Courbin, F., Kneib, J. P., & McCarthy, I. G. 2017, MNRAS, 472, 1972
Harvey, D., Robertson, A., Massey, R., & McCarthy, I. G. 2019, MNRAS, 488, 1572
Heitmann, K., Finkel, H., Pope, A., et al. 2019, ApJS, 245, 16
Hennawi, J. F., Dalal, N., Bode, P., & Ostriker, J. P. 2007, ApJ, 654, 714
Hilbert, S., White, S. D. M., Hartlap, J., & Schneider, P. 2008, MNRAS, 386, 1845
Ho, S., & White, M. 2005, APh, 24, 257
Horesh, A., Ofek, E. O., Maoz, D., et al. 2005, ApJ, 633, 768
Hu, W., & Kravtsov, A. V. 2003, ApJ, 584, 702
Jauzac, M., Richard, J., Limousin, M., et al. 2016, MNRAS, 457, 2029
Johnson, T. L., & Sharon, K. 2016, ApJ, 832, 82
Johnson, T. L., Sharon, K., Bayliss, M. B., et al. 2014, ApJ, 797, 48
Jullo, E., & Kneib, J. P. 2009, MNRAS, 395, 1319
Jullo, E., Kneib, J. P., Limousin, M., et al. 2007, NJPh, 9, 447
Kassiola, A., & Kovner, I. 1993, ApJ, 417, 450
Kawamata, R., Ishigaki, M., Shimasaku, K., et al. 2018, ApJ, 855, 4
Kawamata, R., Oguri, M., Ishigaki, M., Shimasaku, K., & Ouchi, M. 2016, ApJ, 819, 114
Keeton, C. R. 2001, arXiv:astro-ph/0102341
Killedar, M., Borgani, S., Fabjan, D., et al. 2018, MNRAS, 473, 1736
Killedar, M., Borgani, S., Meneghetti, M., et al. 2012, MNRAS, 427, 533
Kneib, J. P., Ellis, R. S., Smail, I., Couch, W. J., & Sharples, R. M. 1996, ApJ, 471, 643
Kneib, J.-P., & Natarajan, P. 2011, A&ARv, 19, 47
Komatsu, E., Smith, K. M., Dunkley, J., et al. 2011, ApJS, 192, 18
Lagattuta, D. J., Richard, J., Bauer, F. E., et al. 2019, MNRAS, 485, 3738
Li, G. L., Mao, S., Jing, Y. P., et al. 2006, MNRAS, 372, L73
Liesenborgs, J., De Rijcke, S., & Dejonghe, H. 2006, MNRAS, 367, 1209
Lotz, J. M., Koekemoer, A., Coe, D., et al. 2017, ApJ, 837, 97
Mahler, G., Richard, J., Clément, B., et al. 2018, MNRAS, 473, 663
Mahler, G., Sharon, K., Fox, C., et al. 2019, ApJ, 873, 96
McCarthy, I. G., Schaye, J., Bird, S., & Le Brun, A. M. C. 2017, MNRAS, 465, 2936
McDonald, M., Allen, S. W., Bayliss, M., et al. 2017, ApJ, 843, 28
Meneghetti, M., Argazzi, R., Pace, F., et al. 2007, A&A, 461, 25
Meneghetti, M., Bartelmann, M., Dahle, H., & Limousin, M. 2013, SSRv, 177, 31
Meneghetti, M., Bartelmann, M., Dolag, K., et al. 2005, A&A, 442, 413
Meneghetti, M., Bartelmann, M., & Moscardini, L. 2003, MNRAS, 340, 105
Meneghetti, M., Yoshida, N., Bartelmann, M., et al. 2001, MNRAS, 325, 435
Meneghetti, M., Natarajan, P., Coe, D., et al. 2017, MNRAS, 472, 3177
Miralda-Escude, J. 1995, ApJ, 438, 514
Mohammed, I., Liesenborgs, J., Saha, P., & Williams, L. L. R. 2014, MNRAS, 439, 2651
Molikawa, K., & Hattori, M. 2001, ApJ, 559, 544
Morioka, M., & Futamase, T. 2015, ApJ, 805, 184
Navarro, J. F., Frenk, C. S., & White, S. D. M. 1997, ApJ, 490, 493
Oguri, M. 2010, PASJ, 62, 1017
Oguri, M., & Blandford, R. D. 2009, MNRAS, 392, 930
Oguri, M., Taruya, A., & Suto, Y. 2001, ApJ, 559, 572
Okabe, T., Oguri, M., Peirani, S., et al. 2020, MNRAS, 496, 2591
Paterno-Mahler, R., Sharon, K., Coe, D., et al. 2018, ApJ, 863, 154
Planck Collaboration, Ade, P. A. R., Aghanim, N., et al. 2016, A&A, 594, A27
Postman, M., Coe, D., Benítez, N., et al. 2012, ApJS, 199, 25
Raney, C. A., Keeton, C. R., & Brennan, S. 2020a, MNRAS, 492, 503
Raney, C. A., Keeton, C. R., Brennan, S., & Fan, H. 2020b, MNRAS, 494, 4771
Redlich, M., Bartelmann, M., Waizmann, J. C., & Fedeli, C. 2012, A&A, 547, A66
Remolina González, J. D., Sharon, K., Li, N., et al. 2021, ApJ, 910, 146
Remolina González, J. D., Sharon, K., & Mahler, G. 2018, ApJ, 863, 60
Richard, J., Smith, G. P., Kneib, J.-P., et al. 2010, MNRAS, 404, 325
Richard, J., Jauzac, M., Limousin, M., et al. 2014, MNRAS, 444, 268
Rozo, E., Nagai, D., Keeton, C., & Kravtsov, A. 2008, ApJ, 687, 22
Ruel, J., Bazin, G., Bayliss, M., et al. 2014, ApJ, 792, 45
Saez, C., Campusano, L. E., Cypriano, E. S., Sodré, L., & Kneib, J. P. 2016, MNRAS, 460, 4453
Salmon, B., Coe, D., Bradley, L., et al. 2020, ApJ, 889, 189
Schaller, M., Dalla Vecchia, C., Schaye, J., et al. 2015a, MNRAS, 454, 2277
Schaller, M., Frenk, C. S., Bower, R. G., et al. 2015b, MNRAS, 452, 343
Sharon, K., Bayliss, M. B., Dahle, H., et al. 2020, ApJS, 247, 12
Smith, G. P., Kneib, J.-P., Smail, I., et al. 2005, MNRAS, 359, 417
Sunyaev, R. A., & Zeldovich, Y. B. 1970, Ap&SS, 7, 3
Torri, E., Meneghetti, M., Bartelmann, M., et al. 2004, MNRAS, 349, 476
Umetsu, K., Broadhurst, T., Zitrin, A., Medezinski, E., & Hsu, L.-Y. 2011, ApJ, 729, 127
Wambsganss, J., Ostriker, J. P., & Bode, P. 2008, ApJ, 676, 753
Williams, L. L. R., & Lewis, G. F. 1998, MNRAS, 294, 299
Wyithe, J. S. B., Turner, E. L., & Spergel, D. N. 2001, ApJ, 555, 504
Xu, B., Postman, M., Meneghetti, M., et al. 2016, ApJ, 817, 85
Zaritsky, D., & Gonzalez, A. H. 2003, ApJ, 584, 691
Zitrin, A., Broadhurst, T., Umetsu, K., et al. 2009, MNRAS, 396, 1985
Zitrin, A., Seitz, S., Monna, A., et al. 2017, ApJL, 839, L11